AN INVESTIGATION OF MICROSTRUCTURE, MICROHARDNESS AND BIOCOMPATIBILITY CHARACTERISTICS OF YTTRIUM HYDROXYAPATITE DOPED WITH FLUORIDE

A THESIS SUBMITTED TO
THE GRADUATE SCHOOL OF NATURAL AND APPLIED SCIENCES
OF
MIDDLE EAST TECHNICAL UNIVERSITY

BY

SIDIKA MİNE TOKER

IN PARTIAL FULLFILLMENT OF THE REQUIREMENTS
FOR
THE DEGREE OF MASTER OF SCIENCE
IN
BIOMEDICAL ENGINEERING

JANUARY 2010

Approval of the thesis:

AN INVESTIGATION OF MICROSTRUCTURE, MICROHARDNESS AND BIOCOMPATIBILITY CHARACTERISTICS OF YTTRIUM HYDROXYAPATITE DOPED WITH FLUORIDE

submitted by **SIDIKA MİNE TOKER** in partial fulfillment of the requirements for the degree of **Master of Science in Biomedical Engineering Department, Middle East Technical University** by,

Prof. Dr. Canan Özgen
Dean, Graduate School of **Natural and Applied Sciences** _____

Prof. Dr. Zülfü Aşık
Head of Department, **Biomedical Engineering** _____

Assoc. Prof. Dr. Zafer Evis
Supervisor, **Engineering Sciences Dept., METU** _____

Assoc. Prof. Dr. Caner Durucan
Co-supervisor**, Metallurgical and Materials Engineering Dept., METU** _____

Examining Committee Members

Prof. Dr. Ahmet N. Eraslan
Engineering Sciences Dept., METU _____

Assoc. Prof. Dr. Zafer Evis
Engineering Sciences Dept., METU _____

Assoc. Prof. Dr. Caner Durucan
Metallurgical and Materials Engineering Dept., METU _____

Assist. Prof. Dr. Dr. Ayşen Tezcaner
Engineering Sciences Dept., METU _____

Assist. Prof. Dr. Dilek Keskin
Engineering Sciences Dept., METU _____

Date: 22.01.2010

I hereby declare that all information in this document has been obtained and presented in accordance with academic rules and ethical conduct. I also declare that, as required by these rules and conduct, I have fully cited and referenced all material and results that are not original to this document.

Name, Last name: Sıdıka Mine Toker

Signature:

ABSTRACT

AN INVESTIGATION OF MICROSTRUCTURE, MICROHARDNESS AND BIOCOMPATIBILITY CHARACTERISTICS OF YTTRIUM HYDROXYAPATITE DOPED WITH FLUORIDE

TOKER, Sıdıka Mine

M. S., Department of Biomedical Engineering

Supervisor: Assoc. Prof. Dr. Zafer Evis

Co-Supervisor: Assoc. Prof. Dr. Caner Durucan

January 2010, pages 92

The aim of this study was to investigate the microstructure, microhardness and biocompatibility properties of nano hydroxyapatite (HA) doped with a constant yttrium (Y^{3+}) and varying fluoride (F^-) compositions. HA was synthesized via precipitation method and sintered at 1100°C for 1 hour. Increased densities were achieved upon Y^{3+} doping while F^- doping led to a decrease in densities. For structural analysis, XRD, SEM and FTIR spectroscopy examinations were performed. No secondary phases were observed in XRD studies upon doping. Lattice parameters decreased due to substitutions of ions. In SEM analysis, addition of doping ions was observed to result in smaller grains. In FTIR analysis, in addition to the characteristic bands of HA, novel bands indicating the substitution of F^- ions were observed in F^- ion doped samples. The highest microhardness value was obtained for the sample doped with 2.5%Y^{3+}, 1%F^-. Increased F^- ion contents resulted in decreased microhardness values.

For biocompatibility evaluation, in vitro tests were applied to the materials. MTT assay was performed for Saos-2 cell proliferation analysis. Y^{3+} and F^- ion incorporation was found to improve cell proliferation on HA discs. Cells were found

to attach and proliferate on disc surfaces in SEM analysis. ALP assay showed differentiation of cells on the discs can be improved by doping HA with an optimum amount of F^- ion. Dissolution tests in DMEM revealed that structural stability of HA was improved with F^- ion incorporation.

The material exhibiting optimum structural, mechanical and biocompatibility properties was HA doped with 2.5%Y^{3+}, 1%F^-.

Keywords: Nano Hydroxyapatite, Fluoride, Yttrium, Microstructure, Microhardness, Biocompatibility.

ÖZ

FLOR İLAVE EDİLMİŞ İTRİYUM HİDROKSİAPATİTİN MİKROYAPI, MİKROSERTLİK VE BİYOUYUMLULUK ÖZELLİKLERİNİN İNCELENMESİ

TOKER Sıdıka Mine

Yüksek Lisans, Biyomedikal Mühendisliği
Tez Yöneticisi: Doç. Dr. Zafer Evis
Yardımcı Tez Yöneticisi: Doç. Dr. Caner Durucan

Ocak 2010, sayfa 92

Bu çalışmanın amacı sabit miktarda itriyum (Y^{3+}) ve değişen miktarlarda flor (F^-) iyonlarıyla zenginleştirilen nano hidroksiapatitin (HA), mikroyapı, mikrosertlik ve biyouyumluluk özelliklerini incelemektir. HA çöktürme metoduyla üretilmiş ve 1100°C'de 1 saat sinterlenmiştir. Y^{3+} eklenmesiyle daha yüksek yoğunluklar elde edilmiş, F^- eklenmesin ise yoğunluklarda azalmaya yol açmıştır. Yapısal inceleme için XRD, SEM ve FTIR spectroskopisi analizleri uygulanmıştır. XRD çalışmalarında iyon ekleme sonucu ikincil fazlara rastlanmamıştır. İyon eklenmesiyle latis paramaterler küçülmüştür. SEM incelemelerinde, eklenen iyonların daha küçük tanecik boyutu sağladığı gözlenmiştir. FTIR analizinde karakteristik HA bantlarına ek olarak, F^- iyonu eklenmiş örneklerde F^- iyonlarının yer değiştirmesi sonucu oluşan yeni bantlar gözlenmiştir. En yüksek mikrosertlik değeri %2.5 Y^{3+}, %1 F^- ile zenginleştirilen örnekte gözlenmiştir. F^- miktarlarının artışı sertlik değerlerinde azalmaya sebep olmuştur.

Biyouyumluluk incelemeleri için malzemelere in vitro testler uygulanmıştır. Saos-2 hücre çoğalması analizi için MTT deneyi uygulanmıştır. Y^{3+} ve F^- iyonları eklenmesinin HA diskleri üzerinde hücre çoğalmasına olumlu etkileri olduğu görülmüştür. SEM incelemelerinde hücrelerin disk yüzeylerine yapışabildikleri ve

çoğalabildikleri gözlenmiştir. ALP analizi HA'e optimum miktarda F^- eklenerek diskler üzerindeki hücre farklılaşmasının artırılabileceğini göstermiştir. DMEM içinde yapılan çözünme testleri F^- iyonu eklenmesinin HA'in yapısal kararlılığını artırdığını göstermiştir.

Optimum yapısal, mekanik ve biyouyumluluk özellikleri gösteren malzeme %2.5 Y^{3+}, %1 F^- ile zenginleştirilen HA'dır.

Anahtar Sözcükler: Nano Hidroksiapatit, Flor, İtriyum, Mikroyapı, Mikrosertlik, Biyouyumluluk.

ACKNOWLEDGEMENTS

I would like to express my appreciation to my advisor Assoc. Prof. Dr. Zafer Evis for his guidance, encouragement and patience throughout this study. I am so grateful to my advisor for letting me benefit from his profound knowledge and experience. I would also like to express my thanks to my co-advisor Assoc. Prof. Dr. Caner Durucan for his guidance starting from my undergraduate studies in this exciting field and his help throughout my thesis.

I owe my special thanks to Assist. Prof. Dr. Ayşen Tezcaner; for her precious guidance, support and patience throughout my thesis; especially through in vitro studies. I also would like to thank Assist. Prof. Dr. Dilek Keskin for the lectures she gave in my graduate courses and her help throughout this study.

I would like to express my gratitude to my advisor Assoc. Prof. Dr. Zafer Evis, Assist. Prof. Dr. Ayşen Tezcaner and Assist. Prof. Dr. Dilek Keskin for their generosities to let me work in their Biomaterials laboratory. I owe my thanks to my lab friends Pınar Sun for her guidance during my experiments, Ayşegül Kavas and Özge Erdemli for their help through in vitro studies and their precious friendship. I also would like to thank my other dear lab friends; İdil Uysal, Yiğit Öcal, Mert Baki, Özlem Aydın, Ömer Aktürk, Aslı Deniz and Aydın Tahmasebifar for their support, friendship and the lovely environment they created in our lab.

I would like to express my special thanks to my dearest and oldest friends Dr. Burcu Azapoğlu and Gülen Göktürk for their precious friendship. With their

presence, the joy they bring into my life and their constant support, they mean more than sisters to me.

I would like to give my greatest thanks to my parents Mithat Toker and Nedret Toker for the values they taught and the endless support they provided through my entire life. Their respect and belief in what I do is precious for me.

Finally, I would like to express my very special thanks and gratitude to my brother, friend and mentor Assist. Prof. Dr. Umut Toker. His presence, his confidence in me, his ideas and constant support have always given me inspiration and the strength I needed at every stage of my life, as in this study.

TABLE OF CONTENTS

LIST OF TABLES

LIST OF FIGURES

LIST OF ABBREVIATIONS

ALP	: Alkaline Phosphatase
AMP	: Adenosine monophosphate
BCA	: Bicinchoninic Acid
DMEM	: Dulbecco's Modified Eagle's Medium
DMSO	: Dimethyl Sulfoxide
FA	: Fluorapatite
FBS	: Fetal Bovine Serum
FHA	: Fluoridated Hydroxyapatite
FTIR	: Fourier Transfer Infrared Spectroscopy
HA	: Hydroxyapatite
JCDPS	: Joint Committee on Powder Diffraction Standards
MTT	: Methylthiazolyldiphenyl-tetrazolium
PBS	: Phosphate Buffer Saline
pNPP	: p-Nitrophenyl Phosphate
SEM	: Scanning Electron Microscopy
TTCP	: Tetracalcium phopshate
α-TCP	: α-Tricalcium Phosphate
β-TCP	: β-Tricalcium Phosphate
XRD	: X-Ray Diffraction

CHAPTER 1

1. INTRODUCTION

1.1 Bone

Bone is the fundamental tissue of the skeletal system, which performs primary functions such as structural support for muscular activity, physical protection for the internal organs and soft tissues, and storage facility for systemic mineral homeostasis [1].

1.1.1 Structure and Mechanical Properties of Bone

Bone can be considered as a natural composite material consisting of organic and inorganic components [2]. Inorganic part makes up 60-70 % of the bone, 5-8 % of the bone consists of water and the organic part makes up the rest. [3]. Organic part of the bone is made up of type I collagen and some non-collageneous matrix proteins. Inorganic part of the bone is mainly hydroxyapatite (HA, $Ca_{10}(PO_4)_6(OH)_2$) whose basic constituents are calcium and phosphate. In addition to these two elements, various elements exist in trace amounts in the structure of HA [4].

Bone has a hierarchical structure that varies from macroscopic to nanoscale levels [5]. These levels and structures are: the macrostructure, which is composed of

cancellous and cortical bone; the microstructure (from 10 to 500 μm), containing Haversian systems, osteons, single trabeculae; the sub-microstructure (1–10 μm), consisting of lamellae; the nanostructure (from a few hundred nanometers to 1μm), containing fibrillar collagen and embedded mineral; and the sub-nanostructure (below a few hundred nanometers), with molecular structure of constituent elements, such as mineral, collagen, and non-collagenous organic proteins [1]. These structures are illustrated in Figure 1.1.

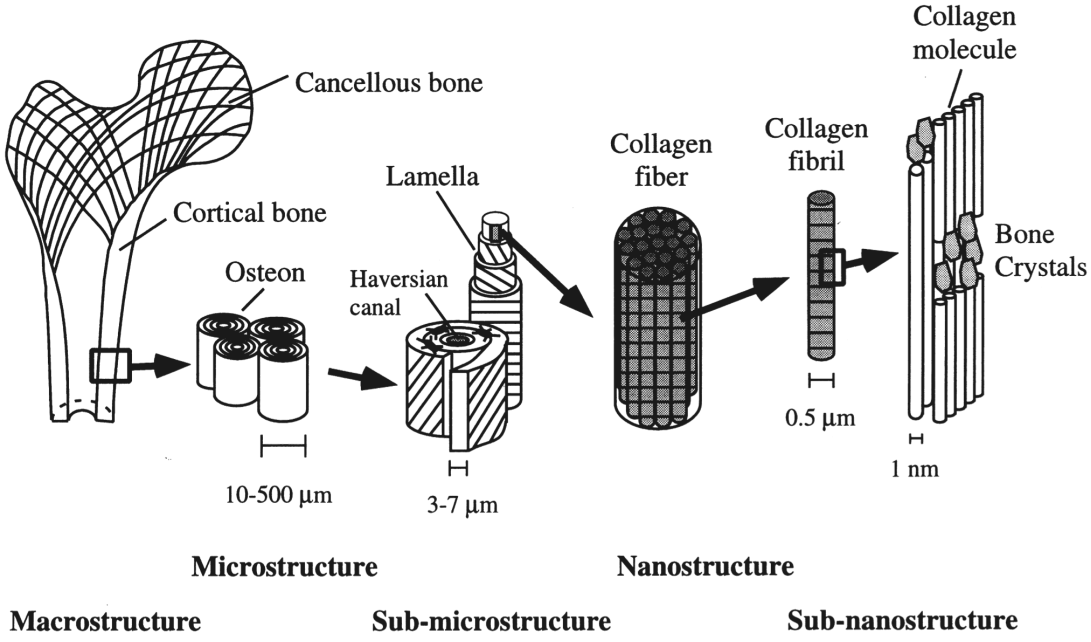

Figure 1.1. Hierarchical structure of the bone [1].

The complicated hierarchical structure of the bone is believed to influence its mechanical properties. At the macrostructural level the main parameter influencing mechanical properties of the bone is its porosity. As mentioned above, bone consists of compact and cancellous bone in macroscopic level. These two structures are distinguished from each other in terms of their levels of porosity.

Compact bone has a more dense structure while cancellous bone exhibits a high level of porosity [1]. Some of the mechanical properties of human cortical and cancellous bones are given in Table 1.1.

Table 1.1. Range of values of mechanical properties of human cortical and cancellous bones [6].

Bone	**Cortical**	**Cancellous**
Axial Modulus of Elasticity (E_{axial}) (GPa)	14 – 27	0.011 – 3.12
$E_{tangenital}$ (Gpa)	7 – 17	0.023 – 1.5
E_{radial} (Gpa)	7 – 16	0.024 – 1.5
Density (ρ) (g/cm^3)	1.545 – 2.118	0.055 – 0.0744
Ultimate Tensile Strength (σ_{UTS}) (Mpa)	150	0.11 – 11

As seen in Table 1.1, cancellous bone has a lower modulus of elasticity compared to that of compact bone due to its greater level of porosity [6, 7].

Although porosity has a negative effect on the stiffness of cancellous bone, it enables metabolic activity at this part of the bone. Thus cancellous bone remains younger compared to compact bone due to active remodeling. The difference arising from the different maturation properties of these two structures influence their mechanical properties [1]. After maturation a decline is observed in tensile strength of cortical bone due to the decrease in bone density [7].

Despite their structural and mechanical differences, it is impractical to think of these two structures as two separate materials since they make up the macrostructure of the bone together. They are present in the bone in different arrangements which make the mechanical properties of the bone vary along different sites of each bone and in different kinds of bones [1]. Thus porosity is an important parameter which induces anisotropy in bone structure.

These data show that macrostructure of the bone is an important parameter in determining the mechanical properties of the bone. However, the fundamental role in determining the macroscopic mechanical properties of the bone may be played by the nanostructure of the bone since composite like properties of the bone are seen in this level [8].

Nanostructure of the bone can be described as staggered mineral platelets (hydroxyapatite) embedded in a collagen matrix [5]. These mineral platelets grow with a specific crystalline orientation in which the *c* axes of the crystals are roughly parallel to the long axes of the collagen fibrils. The average lengths and widths of the platelets are 50*25 nm, which results in a high aspect ratio of the crystals [1].

The orientation of mineral crystals within collagen matrix is illustrated in Figure 1.2. This preferred alignment and the high aspect ratio of the mineral crystals in the collagen matrix cause anisotropy in mechanical properties of the bone [8]. The complicated structure and anisotropic properties of the bone make it difficult to observe its mechanical properties [1, 5, 8], thus some specially developed models are used for making measurements and estimations about the mechanical properties of bone [8]. Examples of these models are Mori-Tanaka model, Halpin-Tsai model,

Hashin-Shtrikman and hill bounds and Voigt and Reuss bounds [8]. These models are mainly used for determining the mechanical properties of composites and in the case of bone they are used for making estimations about the mechanical properties of the bone by providing upper and lower bounds [8]. The findings of the calculations made by these models revealed that Young's modulus of bone varies depending on the directions of mineral platelets being parallel or transverse. It was observed that Young's Modulus of the mineral platelets approach Voigt upper bound in longitudinal direction and Reuss lower bound in transverse direction [8]. It was also seen that shear modulus of the nanostructure of the bone approaches Reuss lower bound. This directional dependence in Young's modulus induces an anisotropy in the Poison's ratio of the bone as well.

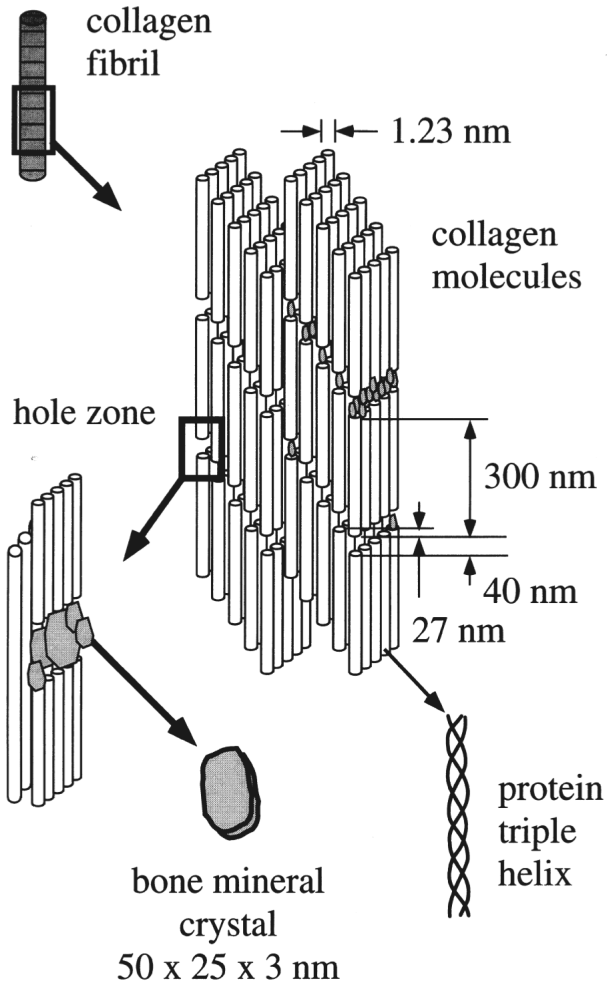

Figure 1.2. Alignment of mineral crystals between collagen fibers [1].

It is seen that in both macro and nano scale that anisotropy plays an important role in determining mechanical properties of the bone. In addition to anisotropy, bone is a viscoelastic material since the dominant collagen phase acts as a viscous material. The limited elasticity and high stiffness of the bone is due to the presence of mineral phase [5]. However, considering its superior mechanical properties and the importance of orientation of mineral platelets in overall bone

mechanics, mineral phase plays an important role in specifying the behavior of the bone in response to applied mechanical forces [2].

Thus, it is important to observe the mechanical properties of hydroxyapatite, which makes up the mineral phase of the bone in order to gain a better understanding of the mechanical behavior of bone.

1.1.2 Presence of Various Elements in Bone Mineral

The main constituent of the mineral part of the bone is HA with various dopings [9]. Studies show that although they exist in trace amounts, these elements contribute to important changes in the mechanical properties of the bone. Some of these studies are discussed below.

In a study conducted on the deer's antler bone, mechanical properties of the antler bone were examined [9]. In this study, antlers from two different groups of deers were observed. The first group was the free ranging group with lower food availability and health unmanaged. The second group was the well fed and health managed captive raised group of deers. These two groups exhibited very similar contents of Ca^{2+} ions, protein and ash; yet there were significant differences in their mechanical properties. Thus, to explain these differences, some other factors were taken into account. The physical (architectural) factors were stated as the differences in cortical thickness and mean shaft diameters of the two groups of antlers and the chemical factors as the variations in the contents of other elements such as Mg, K, Na, Zn, Fe and Si. In Table 1.2, the mentioned differences between the two groups of deers' antlers can be seen.

Table 1.2. Mechanical, architectural and chemical properties of antler bones of two dofferent groups of deers (arbitrary values) [9].

	Free Ranging	**Captive Raised**
Young's modulus E (Gpa)	5.3	6.9
Strength (Mpa)	81.9	103.7
Work to maximum load (kJ/m^2)	18.2	22.2
Cortical Thickness (mm)	4.4	6.0
Mean Shaft Diameter (mm)	35.1	38.9
Ash content (%)	61.6	62.9
Protein (%)	36.7	35.9
Ca (%)	34.4	34.4
Mg (%)	0.81	0.97
Na (%)	0.9	1.2
K (ppm)	600	818
Zn (ppm)	96	87
Fe (ppm)	71	46
Si (ppm)	160	120

After showing the general effects of trace elements on mechanical properties of antler bone, individual effect of each element was also investigated. The findings of this investigation are seen in Table 1.3.

Table 1.3. Individual effects of elements on antler bone mechanical properties [9].

Element	Effect on Strength of the Bone	Effect on Stiffness of the Bone
K	Increased	Decreased
Zn	Decreased	Decreased
Fe	Decreased	Decreased
Si	Decreased	Decreased
Mg	Increased	-
Na	Increased	-

Most of the studies, which investigated the effect of presence of various elements in bone mineral, conducted experiments on rats. In such studies, mainly rat subjects were divided into groups, each group was fed a special diet depending on the element to be studied and the mechanical properties of the bones obtained from these rats were examined. Results of the studies conducted on rats are summarized in Table 1.4.

Uptake of various elements by the bone mineral is a function of the affinity of the particular element for the bone mineral and extracellular matrix. It also depends on the concentration of the element in the plasma and the degree of mineralization of the bone [10]. Effects of some metals on human bone metabolism are summarized in Table 1.5.

Table 1.4. Effect of various elements on the mechanical properties of rat bones [11-15].

Element & Treatment	Effect on Bone Mechanical Properties
Al Supplementation	No significant difference up to yield point Lower post-yield ultimate strength
Fe Deficiency	Lower fracture strength
Cu Deficiency	Lower fracture strength
Zn Deficiency & Supplementation	Reduction in bone strength due to Zn deficiency Improvement in bone size, mass and strength due to Zn supplementation
Se Deficiency & Supplementation	Reduction in bone stiffness, mass and crystallinity in both treated groups
Cd Exposure	Reduction in bone mineral density, yield strength, fracture strength

Table 1.5. Effects of accumulation of some metals on human bone metabolism [10].

Element	Effect
Al	Inhibit mineralization. Act as bone cells.
B	No change in B level of the bone after diet. Increase in vertebral resistance to crush force.
Cd	Diminish mineralization ability of bone cells negatively. Accelerate bone resorption . Induce calcium deficiency.
Pb	Replace Ca in bone and decrease Ca level of the blood. Majorly stored in the skeleton.
Si	Increase in femoral bone mineral density.
Sr	Replaces Ca, represses Ca metabolism. High intake causes rickets, poor bone formation and mineralization.

1.2 Bioceramics

The use of bioceramics has been expanded due to the advantages they offer for orthopedic applications [16, 17]. Some bioceramics like alumina and zirconia have outstanding mechanical properties while some bioceramics like calcium phosphates are preferred due to their similarity to the bone mineral. These properties of bioceramics are discussed below.

According to the interaction between the host and the implant, bioceramics can be classified as bioinert or bioactive. Bioactive ceramics can be further

classified as resorbable or non-resorbable [16, 17]. These categories are summarized in Table 1.6, with an example to each category.

Table 1.6. Classification of various bioceramics due to host response [17].

Category	**Example**
Bioinert	Alumina (Al_2O_3)
Resorbable	Tricalcium phosphate (TCP) ($Ca_3(PO_4)_2$)
Non-resorbable (Surface Reactive)	Bioglass

Bioceramics can also be classified according to their main chemical constituents. In Table 1.7, some common types of bioceramics are given with their various properties and possible biomedical applications.

Table 1.7. Properties and biomedical applications of various bioceramics [16 – 18].

Bioceramic	**Properties**	**Biomedical Applications**
Alumina (Al_2O_3)	Good mechanical properties Modest fracture toughness High wear resistance Good biocompatibility Excellent corrosion resistance	Hip prosthesis Knee prosthesis Dental implants Bone screws Middle ear bone substitutes
Zirconia (ZrO_2)	Highest fracture toughness among monolithic ceramics Superior wear performance compared to alumina and metals	Hip prosthesis

Tablo 1.7 cont'd. Properties and biomedical applications of various bioceramics [16 – 18].

Calcium Phosphates	TCP ($Ca_3(PO_4)_2$)	Biodegradable Thermodynamically stable at elevated temperatures	Orthopedics Bone substitutes Drug delivery
	Hydroxyapatite	Bioactive Stable at physiological pH and temperature Relatively lower strength and toughness	Coatings for orthopedic and dental implants Bone tissue substitutes Drug delivery
	Tetracalcium phosphate (TTCP) ($Ca_4(PO_4)_2°$)	High solubility in water	Self setting cements
Bioglasses		Ease of shaping Fine grained microstructure Optimal mechanical properties Good mechanical and thermal shock resistance	Middle ear bone substitutes Pelvic bone replacement Vertebral surgery

1.3 Calcium Phosphates

Since the mineral part of the bone is a HA with a high bioactivity in the body, calcium phosphates become desirable in biomedical applications. As presented in Table 1.7, there are various kinds of calcium phosphates with different material properties.

Ca/P ratios of these materials influence their properties at different aspects [16]. For instance, if the Ca/P ratio of HA is lower than 1.67, α or β-TCP phases may appear after processing. If Ca/P ratio is higher than 1.67, calcium oxide (CaO) may appear with HA. The presence of these secondary phases may affect the biological properties of the material. TCP, whose Ca/P ratio is 1.5, has a higher resorption rate than that of HA [16]. The Ca/P ratios of some calcium phosphates are shown in Table 1.8.

Table 1.8. Ca/P ratios of some calcium phosphates [18].

Phase	Ca/P ratio
HA	1.67
TCP	1.5
TTCP	2

Different calcium phosphates are used for different biomedical applications, depending on the bioactivity or resorption rates of the material. However, the limitation for the use of calcium phosphates is their poor mechanical properties [18]. Improving the mechanical properties of calcium phosphates are possible, ways of which are discussed in the following chapters.

Among the calcium phosphates, HA is more widely used when compared to other calcium phosphates owing to its stability in physiological environment and bioactivity.

1.4 Hydroxyapatite

HA has been widely used in orthopedic applications such as coatings and bone substitutes, due to its chemical resemblance to natural bone mineral [16,18]. HA can be used in powder or particulate form depending on the application [18]. Some of the important details about HA are discussed below.

1.4.1 Synthesis Methods of Hydroxyapatite

There are a number of synthesis methods present for the production of HA. These methods are given in Table 1.9.

Table 1.9. Various synthesis methods of HA [19 – 27].

HA Synthesis Method
Solid state reactions
Precipitation method
Hydrothermal reactions
Emulsion and micro-emulsion techniques
Sol–gel synthesis

1.4.1.1 Solid State Reactions

In the synthesis of HA by solid-state reactions, first a mixture of inorganic components is prepared with the use of acetone or water [19, 20]. The mixture is then milled, dried and heat treated [19, 20]. Milling is an important parameter in

solid state sintering since this parameter has an effect on both water adsorption and surface area of the powders, thus it influences the powder size of the product [20]. Milling also induces the risk of contamination in the product [20]. Heat treatment is another parameter in this method since structural transitions are seen during heat treatment [19, 20].

According to the findings of the structural and mechanical characterization processes and biocompatibility analysis, HA produced by solid state sintering exhibits good mechanical properties and good biocompatibility [19]. Although density of this material is close to natural bone density, its hardness values are very high compared to that of natural bone [19]. Also it is difficult to obtain single phase HA with this method since phase transitions are seen during thermal processing [19]. In this method, formation of a single phase highly crystalline HA becomes possible by increasing water adsorption during milling [20]. Thus solid state sintering can be suitable for mass production of high crystalline HA, since it is an economical and simple method despite its disadvantages [20].

1.4.1.2 Emulsion and Micro-emulsion Techniques

In microemulsion and emulsion techniques, HA powders are produced by reacting calcium chloride ($CaCI_2$) with $(NH_4)_2HPO_4$. The reactions are performed by the use of different ratios of cyclohexane surfactant, which determine whether the solution acts as a bicontinuous microemulsion, inverse microemulsion or emulsion structure [21]. Bicontinuous and inverse microemulsion lead to formation of nano-sized and highly sinterable HA powder while the HA powder that is

produced via emulsion exhibits larger grain size compared to the two microemulsion methods [21]. The microemulsion techniques can also be considered advantageous in terms of providing nano-sized and processible HA powders.

1.4.1.3 Hydrothermal Reactions

In hydrothermal synthesis of HA, dicalcium phosphate dihydrate ($CaHPO_4 \cdot 2H_2O$) powders are mixed with calcium carbonate ($CaCO_3$) or calcium hydroxide ($Ca(OH)_2$) [22, 23]. In the case of mixing $CaHPO_4 \cdot 2H_2O$ with $CaCO_3$, the mixture is prepared at Ca/P ratios of 1.0 and 1.67 [22]. The mixtures are then hydrolyzed in a NaOH solution and filtered to separate aggregates [22]. The obtained powders are heat treated at various temperatures and it is observed that increasing the temperature affected the grain size and led to formation of new phases for both Ca/P ratios, while it affects the crystallinity only for the specimen with a Ca/P ratio of 1.0 [22].

In the second case, powders of $CaHPO_4 \cdot 2H_2O$ and $Ca(OH)_2$ are heated with distilled water in a pressurized pot which resulted in HA powders of good crystallinity, good sinterability, high strength and biocompatibility [23]. This method is also advantageous in terms of low cost [23].

1.4.1.4 Sol-gel Synthesis

Sol gel method offers a molecular level mixing of the calcium and phosphorus, by which chemical homogeneity is improved and synthesis temperature

is reduced compared to conventional methods [18, 24]. In Figure 1.3, the experimental procedure of HA synthesis by a simple sol-gel method is seen [24].

Crystalline degree, morphology and the particle size of HA obtained by the sol-gel synthesis depends on sintering temperature and time [24, 25].

Apart from its simplicity, sol-gel synthesis of HA is similar to other methods of HA production in terms of controlling grain size and morphology with sintering temperature [24 – 26].

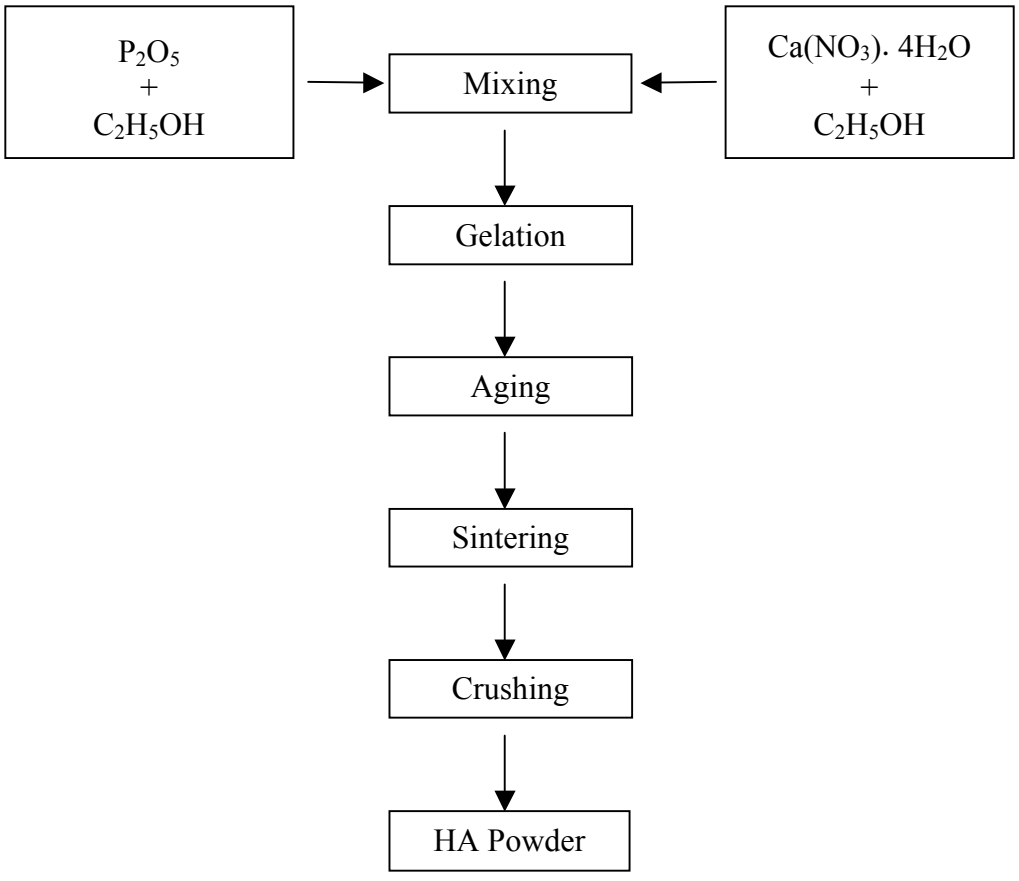

Figure 1.3. Flow sheet for the experimental procedure of HA synthesis by sol-gel method [24].

1.4.1.5 Precipitation Method

Precipitation method is a wet production method of HA. In this method, HA is prepared by calcium nitrate tetra hydrate $Ca(NO_3)_2{\cdot}4H_2O$) and di-ammonium hydrogen phosphate ($(NH_4)_2HPO_4$) as the starting materials with the use of ammonia for pH adjustment [27]. Two separate solutions are prepared, one using calcium nitrate tetra hydrate with distilled water and the other one using di-ammonium hydrogen phosphate with distilled water. These mixtures are stirred at 25°C. After stirring, di-ammonium hydrogen phosphate in distilled water solution is added dropwise into calcium nitrate tetra hydrate in distilled water solution as ammonia is added into for pH adjustment. The pH of the final solution is adjusted to be 11. Formation of HA by this method is explained by the following reaction [27]:

$$10Ca(NO_3)_2{\cdot}4H_2O + 6(NH_4)_2HPO_4 + 8NH_4OH \rightarrow Ca_{10}(PO_4)_6(OH)_2 + 20NH_4NO_3 + 20H_2O \quad (1.1)$$

The obtained HA precipitate is removed from the solution by filtering and/or centrifugation [27]. The precipitate is then dried, calcined and sintered. It has been observed that heat treatment on HA that is produced by precipitation method does not cause formation of new phases other than HA, while it has an effect on grain size of the product [27]. It was found that increasing the temperature causes an increase in the grain size [27]. These findings show that it is possible to control the grain size of HA produced by precipitation method and obtain nano-sized crystals by applying heat treatment at a suitable temperature. Obtaining the nano-sized HA

crystals is important in biomedical applications due to its increased bioactivity and osseointegration [28, 29]. Thus, precipitation method is promising for synthesis of HA, especially for HA to be used in biomedical field.

1.4.2 Crystal Structure of Hydroxyapatite

HA exhibits a hexagonal structure belonging to the space group $P6_3/m$, which is characterized by a six fold c-axis perpendicular to three a-axes (a_1, a_2, a_3,) 120° angles to each other [30, 31]. The unit cell of HA consists of Ca, PO_4 and OH groups packed in a certain orientation shown in Figure 1.4 [32].

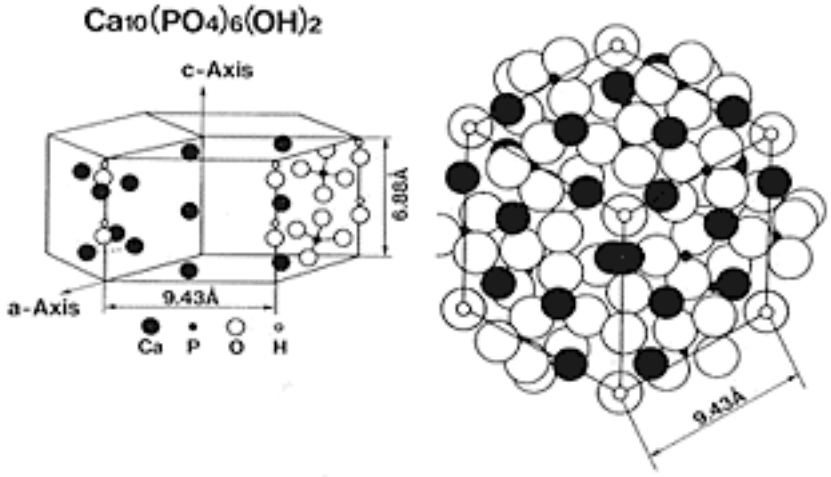

Figure 1.4. Sketch of crystal structure of hydroxyapatite [32].

Ca atoms are present in two different positions in HA structure. Four of the ten Ca atoms occupy Ca (I) position, two at level z=0 and two at z=0.5. The remaining six calcium atoms occupy the Ca (II) position, three at z=0.25 and three at z=0.75, surrounding the OH groups located at the corners of the unit cell (Figure

1.5) [30, 33, 34]. The six (PO_4) groups exhibit a helical arrangement from levels z= 0.25 to z=0.75. This network formed by the (PO_4) groups provides skeletal stability in the HA structure.

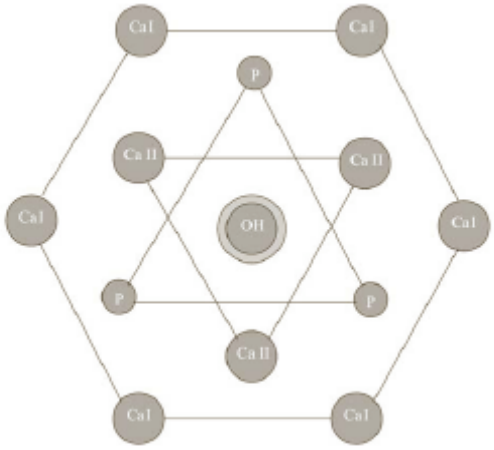

Figure 1.5: Sketch of the relative positions of Ca(I) and Ca (II) atoms in the crystal structure of HA [33].

1.4.3 Phase Transformations of Hydroxyapatite

Phase transformations commonly occur during sintering of HA at high temperatures [35]. In Table 1.10, phase transformations of HA that are seen in different synthesis methods at various temperatures are given.

Table 1.10. Phase transformations of HA seen in different synthesis methods at various temperatures [19, 21-24, 36].

Synthesis Method	**Newly Formed Phase**	**Formation Temperature**
	β-$Ca_2P_2O_7$ & $CaP(HPO_4)(PO_4)_5OH$	500°C
Solid State Reactions	β-TCP	800°C
	α-TCP	1250°C
Microemulsion	β-TCP	1200°C
Sol-gel Sytnhesis	β-TCP & CaO	Above 800°C
Precipitation	β-TCP	Above 1300°C
Hydrothermal Synthesis	-	

In the sintering of sol-gel synthesized HA, formation of β -TCP and CaO phases above 800°C is explained by the following reaction [24]:

$$Ca_{10}(PO_4)_6(OH)_2 \rightarrow 3Ca_3(PO_4)_2 + CaO + H_2O \quad (1.2)$$

However, HA sintered by precipitation method resists to decomposition at 1100°C for several hours [27].

In hydrothermal synthesis of HA, two reactions are expected to occur during sintering [23]:

$$Ca_{10}(PO_4)_6(OH)_2 \rightarrow Ca_{10}(PO_4)_6(OH)_{2-2x}O_x\square_x + xH_2O \quad (1.3)$$

($\square$: non-charged vacancy, $x < 1$)

$$Ca_{10}(PO_4)_6(OH)_2 \rightarrow 2Ca_3(PO_4)_2 + Ca_4P_2O_4 + H_2O \quad (1.4)$$

In the above study [23], these two decomposition reactions did not take place even though a special moisturizing atmosphere was not provided for sintering which was thought to be due to the humidity in the air [23].

In addition to the sintering temperature, calcium deficiency of the synthetic apatite is another factor causing the phase transformations [35]. Deviations from the Ca/P ratio of stoichiometric HA which is 1.67 induces formation of new phases [16, 35].

These studies show the importance of sintering temperature, atmosphere and Ca/P ratio of HA for phase transformations.

1.4.4 Mechanical Properties of Hydroxyapatite

Despite its improved chemical and biological properties, HA is not mechanically stable for load bearing applications. In addition, mechanical properties of HA may not match with those of bone. In Table 1.10, a comparison is made about the mechanical properties of bone and HA [7, 19].

The values of mechanical properties of HA presented in Table 1.11 belong to HA samples produced via solid state reactions which are cold pressed at a pressure of 135 MPa and sintered twice at 1250°C [19]. It was showed that these

values increased as the sintering temperature and compaction pressure increased [19].

In a study, the flexural strength of HA produced via hydrothermal methods was found to be 120 MPa at a sintering temperature of 1200°C [23]. In another study in which HA was produced by sol-gel synthesis, flexural strength was found to be around 58 and 80 MPa depending on the pressing geometry and load applied to the powders, at a sintering temperature of 1250°C [37].

Table 1.11. Comparison of mechanical properties of HA and bone [6, 7, 19].

Materials	**Ultimate Tensile Strength (MPa)**	**Ultimate Compressive Strength (MPa)**	**Modulus of Elasticity (GPa)**
Cortical Bone (Longitudinal)	133	193	17
Cortical Bone (Transverse)	51	33	11.5
Trabecular Bone	3	6	0.961
HA	120	270	20

In a study where three hydroxyapatite samples with different Ca/P ratios were compared, stoichiometric HA was found to have the lowest compressive strength (58 MPa) due to its high porosity level (23.2 %). The HA sample with a Ca/P ratio of 1.65 and porosity level of 6.5 % was found to have the highest compressive strength (108 MPa) among the three samples. The third HA sample which was calcium deficient had a Ca/P ratio of 1.58. That sample had a porosity

level of 10.6 % and a compressive strength of 87 MPa. This study shows the dependence of compressive strength on porosity of the material [38].

In another study HA nanopowders with controlled morphology were synthesized and effect of addition of rod-shaped particles into spherical nanopowders was observed [39]. It was seen that increase in amount of rod-shaped particles caused a decrease in microhardness and an increase in indentation fracture toughness of the samples. In SEM pictures of these samples, an increase in porosity is observed with the addition of rod-shaped particles. This explains the reported mechanical properties such that increased porosity limits crack propagation and increases indentation fracture toughness while it results in lower microhardness values.

These studies show that mechanical properties of HA depend on synthesis methods, heat treatment temperature, porosity, microstructure and stoichiometry of the sample. Thus, lots of variables should be taken into account while producing HA in order to obtain optimum mechanical properties for HA details of which are discussed earlier.

1.4.5 Biological Properties of Hydroxyapatite

HA is a thermodynamically stable material to be used in physiological pH, temperature and composition [18]. It is also crystallographically similar to bone mineral, which induces bone growth on the material [40].

Another decent property of HA is its resorption rate. For implants, it is desirable to be resorbed by the bone after assisting bone repair [16]. This can be

achieved by matching implant resorption rate with bone regeneration rate [16]. This becomes possible by using a mixture of HA with tri-calcium phosphate (TCP) which dissolves much faster than HA [16].

Cell behaviors on HA like adhesion, proliferation, morphology are also important parameters for the bioactivity of HA. In a study morphology and resorption activity of osteoclast-like cells on conventional and nanophase HA and alumina were investigated [28]. In this study the cellular activity of the osteoclast-like cells was determined by the synthesis of tartrate resistant acid phopshatase (TRAP) and the resorption pits formed on material surfaces by the cells. In this study it was observed that for a 13-day time period, TRAP synthesis was the highest on conventional and nanophase HA. For all time periods higher TRAP synthesis was observed on nanophase materials, the highest activity being observed on nanophase HA. For the formation of resorption pits, both conventional and nanophase HA exhibited a similar behavior to the bone reference material, however a higher resoption activity was observed on nanophase HA. This study showed that higher osteoclast-like cell function was observed on nanophase HA compared to conventional HA, which can be explained by the increased roughness, higher surface wettability and the improved solubility of nanophase HA.

In another study, osteoblast functions like proliferation, alkaline phosphatase synthesis and extracellular matrix calcium concentration on various nanophase ceramics including HA were investigated [29]. All the observed osteoblast cell functions were greater on nanophase HA with longer cell culture periods compared to conventional HA.

These two studies demonstrate nanophase HA offers improved biological properties by enhancing osteoclast and osteoblast cell activity on the material.

Another way of improving biological properties of HA is doping it with various elements. This concept is discussed in detail in following sections.

1.4.6 Doping of Hydroxyapatite with Various Ions

Various elements are present in the structure of bone mineral. Moreover, it has also been shown that HA has poor mechanical properties for load bearing applications. Thus, in order to alter its mechanical properties and increase its similarity to natural bone mineral, HA has been doped with various.

Some of these ions are Mg^{2+}, Na^{+}, K^{+}, F^{-}, Y^{3+}, Zn^{2+} ,Cd^{2+}, Sr^{2+}, Ba^{2+}, Pb^{4+}, Cl^{-} ,As^{3-}, V^{5+}, La^{3+}, In^{3+} and Bi^{3+} [33, 41 - 43]. Considering HA to have the chemical formula; $Ca_{10}(PO_4)_6OH_2$, the available site for each doping element is shown in Table 1.12.

Table 1.12. Available sites for doping elements in HA structure [33, 41 - 43].

Available Site	**Doping Element**
Ca	Mg, Zn, Y, In, Na, K, Sr, Pb, Cd, Ba, Bi, Cu
P	As, V
OH	F, Cl

Substitutions of elements to HA may cause changes in lattice parameters, morphology or solubility of HA without changing its hexagonal symmetry [30]. If

the doping elements have the same hexagonal crystal structure of the element they are substituting, they fit into the HA structure. However, depending on the ion size, the doping elements may cause expansion or contraction in the structure of HA [26]. In Table 1.13, ionic radii of some of the doping elements and their effects on lattice parameters and crystallinity of HA are shown [30].

Table 1.13. Ionic radii and effects on lattice parameters and crystallinty of some doping elements [30].

Substituent	**Ionic Radius (A)**	**Lattice Parameters**		**Crystallinty**
		a-axis	c-axis	
For Ca^{2+}	0.99	9.348	6.882	
Sr^{2+}	1.12	increase	increase	no change
Ba^{2+}	1.34	increase	increase	decrease
Pb^{+}	1.20	increase	increase	decrease
K^{+}	1.33	no change	no change	no change
Na^{+}	0.97	no change	no change	no change
Li^{+}	0.68	no change	no change	no change
Mg^{2+}	0.66	decrease**	decrease**	decrease**
Cd^{2+}	0.97	decrease	decrease	decrease
Mn^{2+}	0.80	decrease	decrease	decrease
Zn^{2+}	0.74	increase**	increase**	decrease**
Al^{3+}	0.51	increase	increase	decrease
For OH^{-}	1.34			
F^{-}	1.36	decrease	no change	increase
Cl^{-}	1.81	increase	decrease	no change

**TCP formed [30]

In a study [42], structural properties of HA doped with Mg^{2+}, Cd^{2+}, Zn^{2+} and Y^{3+} ions were investigated. No second phases appeared with the substitution of these ions in this study. A decrease in both lattice parameters 'a' and 'c', and a shrinkage in hexagonal lattice volume was observed for the doped HA samples. This shrinkage was considered to be normal since ionic radii of the cations used in this study were smaller compared to that of Ca^{2+} ion. Grain sizes of all the doped samples were found to be smaller than that of pure HA, except for the HA sample doped with Cd^{2+} ions. This study showed that these ions incorporated in the HA structure in solid solution. It is known that the divalent Mg^{2+}, Cd^{2+} and Zn^{2+} ions substituted for Ca^{2+} ions in HA structure. This study suggests that the trivalent Y^{3+} ion also substitutes for Ca^{2+} ion. Details of the Y^{3+} related part of this study is discussed in the next chapter.

In another study [44], effects of Mg^{2+} and Si^{4+} ions incorporation into HA are investigated. In this study, it was observed that P^{5+} ions were replaced by Si^{4+} ions, which caused an increase in the lattice constants due to the larger ionic size of Si^{4+} ions. On the contrary, replacement of Ca^{2+} ions by Mg^{2+} ions caused a decrease in the lattice constants due to the relatively smaller ionic radius of Mg^{2+} ion. Co-substitution of Mg^{2+} and Si^{4+} ions into HA resulted in an overall decrease in the lattice constants of HA, which proves the structural incorporation of these ions in HA. In this study, HA samples were substituted by Si^{4+} ion alone and co-substituted by Si^{4+} and Mg^{2+} ions. Only Si^{4+} substituted samples were found to be thermally stable up to 1200°C at a substitution level of less than 1.97 weight % Si. The co-substituted samples remained their thermal stability at 1200°C up to a doping level

of 1 weight % of each element. Si substituted samples were found to consist of mono-phase HA grains up to a substitution level of 1.97 weight %. In co-substituted samples, Mg substitution was found to result in destabilization of HA and limit Si substitution at 1.05 weight %. In cell proliferation experiments, both just Si^{4+} ion substituted and co-substituted samples showed biocompatibility.

In a different study [45], HA was doped with divalent Mg^{2+}, Zn^{2+} and trivalent La^{3+}, Y^{3+}, In^{3+}, Bi^{3+} ions; all of which substituted for Ca^{2+} ion site. Lattice parameter information obtained from XRD analysis showed that, cations smaller than Ca^{2+} (Mg^{2+}, Zn^{2+}, Y^{3+}, In^{3+}) resulted in shrinkage in the crystal volume; while cations larger than Ca^{2+} (Bi^{3+}, La^{3+}) caused an increase in the crystal volume, as in the previously discussed studies. This study showed that trivalent ions could also substitute for Ca^{2+} ion. In biocompatibility assays, enhanced osteoblast adhesion and differentiation behaviors were observed for all doped HA samples. Osteoblast response to trivalent ion doped HA was faster compared to divalent ion doped HA. Mineral deposition was found to be more effective in HA samples doped with Zn^{2+}, In^{3+} and Bi^{3+}. Among these three samples, Bi^{3+} doped HA was found to be the best choice in terms of biocompatibility.

1.4.7 Doping of Hydroxyapatite with Yttrium

Among the various ions that HA is doped with, there have been limited studies about doping of HA with yttrium. Although Y^{3+} is a trivalent cation, in the previously discussed studies [41, 42] it was found to substitute for the divalent Ca^{2+} ion site. It was suggested that, the excessive positive charge resulting from the

substitution of Y^{3+} ions are compensated by formation of a calcium ion vacancy for each yttrium ion [41]. In the same study, it was also shown that increasing the Y^{3+} content results in enhanced bulk porosity of the HA samples. In that study, solubility of Y^{3+} in HA was found to be 7% greater. The undissolved Y^{3+} is found to be segregated on HA surface, which could be a possible site for protein adsorption.

This argument is supported in the companion study [45], in which protein adsorption on Y^{3+} doped HA samples are observed. In this study, adsorption of vitronectin and collagen proteins on doped and undoped HA samples were compared. It was found that Y^{3+} doped samples adsorbed greater amounts vitronectin and collagen proteins, which are known to enhance osteoblast adhesion on sample surfaces. This demonstrates that Y^{3+} doped HA provides greater osteoblast adhesion compared to undoped and other doped HA samples. Increased calcium adsorption of Y^{3+} doped HA was explained by the different charge state and structure of Y^{3+} compared to other doping ions, and the rough surface created by Y segregation.

In another study [46], properties of HA coatings on titanium were investigated in terms of osteoblast functions. The coatings were produced from pure and Y^{3+}doped HA powders consisting of nano crystallites. The findings of this study revealed that in Y^{3+}-doped HA coatings, calcium deposition of osteoblasts were enhanced which verifies the findings of the previous study [45].

In a study [36], structural, mechanical and biocompatibility properties of nano HA doped with Y^{3+} and F^{-} were investigated. Structural investigations showed that higher amounts of doping caused decrease in relative density, which could be

compensated by increasing sintering temperature. However, it was seen that higher amounts of Y^{3+} doping and higher sintering temperatures resulted in formation of second phases. In microstructural analyses, it was observed that doping of HA with Y^{3+} and F^- resulted in a decrease in lattice parameters, unit cell volumes and grain size of HA. Mechanical tests showed that doped samples mostly had higher diametral strength compared to undoped samples. Microhardness values showed variations depending on doping amount and sintering temperature. In biocompatibility investigations, doped samples were found to have better cell attachment efficiency. In cell proliferation tests, it was seen that in addition to doping amount, sintering temperature also affected cell proliferation. It was seen that for obtaining the optimum mechanical and microstructural properties, some limitations in doping amount and sintering temperature should be applied. In this study the most outstanding material was found to be HA doped with 2.5 % Y^{3+} and 2.5 % F^- and sintered at 1100°C in terms of its biocompatibility, microstructural and mechanical properties.

These studies showed the importance of Y^{3+} ion substitution into HA, especially in terms of biocompatibility.

1.4.8 Doping of Hydroxyapatite with Fluoride

As presented in Table 1.12, F^- ions substitute for the site OH^- ions in HA structure. If OH^- ions are partially replaced with F^- ions, the obtained material is called fluoridated hydroxyapatite (FHA; $Ca_5(PO_4)_3(OH)_{1-x}F_x$ $0 \leq x \leq 1$). If OH^- ions are completely replaced with F^- ions, fluorapatite (FA; $Ca_5(PO_4)_3F$) is obtained [47,

48]. Controlling the F^- content of HA is an important issue because despite its favorable effects on bone formation and ability to improve mechanical properties of HA, excess amounts of F^- ions could have adverse effects for the bone such as osteomalacia or decreasing osteo-conductivity [47-49].

In a study [47], nano HA, FHA ad FA are produced by wet chemical technique and the obtained materials are mechanically and biologically tested. In XRD analysis, formation of secondary phases was not observed in any of the samples at a sintering temperature up to 1200°C. FTIR results confirmed the replacement of OH^- ions by F^- ions. In TEM analysis, lattice parameters were observed to decrease with increasing the F^- doping. In vitro experiments of this study revealed that increased F^- content of HA could affect cell behavior in two ways: high F^- content enhances cell attachment on HA surface however decrease in Ca^{+2} ion release caused by the increase in F^- content inhibited cell proliferation.

In another study [48], biological effects of F^- release from FHA produced was investigated. FHA samples with varying F^- were produced via pH-cycling method. Cell attachment on FHA discs was tested by contact angle studies and cell culture experiments. In contact angle studies, high F containing discs were found to have lower contact angles, thus lower protein adsorption. This explained by the removal of OH^- ions, which provided binding sites for protein adsorption. However in cell culture studies, although a similar result is obtained for the first 2 hours of cell attachment, later observations showed that, with increasing time of cell culturing, higher amounts of cell attachment was observed on FHA discs compared to pure HA discs. These results suggested that, with increasing cell culture time

more F^- ions were released into the cell culture medium, which promoted cell attachment. In cell proliferation studies, increased F^- was also found to stimulate cell proliferation.

In a study [50], mechanical properties of hydroxyflourapatites – hydroxyapatites in which hydroxyl groups were replaced by F^- ions at F levels of 0%, 20%, 40%, 60%, 80% and 100% were investigated. Hardness, elastic modulus, fracture toughness and brittleness of the samples were measured by microindentation. In hardness measurements, no change was observed until 80% F^- doped HA, after which a rapid increase was observed. A linear increase was observed in elastic modulus with increasing F^- content. Fracture toughness was improved by F^- doping up to an incorporation of 60%, after which a decrease in fracture toughness was observed. The lowest brittleness value was observed for the 60% F^- containing samples and this value also increased after 60% doping with F^-. This study showed that, up to a certain level F incorporation favors mechanical properties if HA while high F levels cause adverse results in terms of mechanical behavior. Thus, for optimum mechanical properties F^- content of doped HAs should not exceed a certain value.

These studies investigating the doping of HA by F^- ion showed that, F^- ion incorporation can improve both mechanical and biological properties of HA as long as optimum levels of doping are achieved.

1.5 Aim of the Study

The purpose of this study is to investigate the mechanical, microstrucural and biocompatibility properties of nano HA doped with Y^{3+} and F^{-} in order to obtain nano HA with improved mechanical and biological properties. Pure and doped HA were synthesized by precipitation method and sintered. Presence of phases and bonding properties of the samples were investigated by X-Ray diffraction (XRD) and Fourier Transform Infrared (FTIR) analysis. Microstructure of the samples was observed with Scanning Electron Microscopy (SEM). For the mechanical investigation, microhardness test was applied to the samples.

For the biocompatibility analysis, in vitro tests were performed using Saos-2 cells. MTT viability tests were applied to cells seeded on pure and doped HA discs for the measurement of cell proliferation. Morphology of the cells on HA discs were investigated by SEM. For the analysis of osteogenic activity of the cells, alkaline phopshatase (ALP) assay was applied. Finally dissolution of HA in Dulbecco's Modified Eagle Medium (DMEM) was examined.

CHAPTER 2

2. MATERIALS AND METHODS

2.1 Materials

2.1.1 Precursors Used For HA Synthesis

Calcium nitrate tetra hydrate ($Ca(NO_3)_2 \cdot 4H_2O$) and di-ammonium hydrogen phosphate ($(NH_4)_2HPO_4$) (Merck, Germany) were the main precursors used for the synthesis of HA. In the synthesis yttrium and fluorine doped HAs, yttrium nitrate ($Y(NO_3)_3 \cdot 6H_2O$) and ammonium fluoride (NH_4F) (Sigma-Aldrich, USA) were used. Ammonia (NH_3) solution (Merck, Germany) was also for the pH adjustment of solutions during synthesis.

2.1.2 Cell Culture Studies

Dulbecco's Modified Eagle Medium (DMEM) (high and low glucose) and fetal bovine serum (FBS) were obtained from Biochrom, Germany. L-ascorbic acid, β-gleycerophosphate, dexamethasone, sodium azide (NaN_3), triton X-100, p-nitrophenyl phosphate (pNPP) substrate solution, bicinchoninic acid solution, cupric sulfate pentahydrate and o-cresolphathalein complexone were the products of Sigma, USA. Penicilin-streptomycin, sodium pyruvate solution, bovine serum albumin and trypsin-EDTA obtained from PAA laboratories GmbH, Austria.

Dimethly sulfoxide (DMSO) (molecular biology grade) was purchased from AppliChem, Germany. Methylthiazolyldiphenyl-tetrazolium (MTT) bromide, glutaraldehyde and Adenosine mono phosphate (AMP) were products of Sigma-Aldrich, Germany. 96 % ethanol and 37 % hydrochloric acid (HCl) were purchased from Ryssen (France) and Merck (Germany), respectively. Calcium carbonate was obtained from Fluka Chemical GmbH Switzerland.

2.2 Methods

2.2.1 Synthesis of HA Samples

2.2.1.1 Synthesis of Pure HA

Precipitation method was used in the synthesis of HA powders [27]. The main precursors were calcium nitrate tetra hydrate ($Ca(NO_3)_2{\cdot}4H_2O$) and di-ammonium hydrogen phosphate ($(NH_4)_2HPO_4$). These two main precursors were added into distilled water in order to prepare 0.6 M ($Ca(NO_3)_2{\cdot}4H_2O$) and 0.3 M $(NH_4)_2HPO_4$. The Ca/P ratio was aimed to be 1.67. After stirring these two solutions for 1 hour, ammonia was added into the di-ammonium hydrogen phosphate solution. After stirring for 10 minutes, ammonia and calcium nitrate solutions were added simultaneously into the di-ammonium hydrogen phosphate–ammonia mixture in a drop wise manner. The aim of using ammonia was to adjust the pH of the final mixture to 11-12. The final mixture was then heated until boiling in order to speed up the reaction. After boiling the mixture was kept being stirred overnight. Following the overnight stirring, the mixture was left to aging for two

days. After the aging process, the mixture was filtered with fine filter paper to obtain a wet cake. The wet cake was dried in the furnace at 200°C to remove the excess water. After drying, the sample was sintered at 1100°C for 1 hour.

2.2.1.2 Synthesis of Doped HAs

In addition to the main precursors used in the synthesis of pure HA, yttrium nitrate ($Y(NO_3)_3 \cdot 6H_2O$) and ammonium fluoride (NH_4F) were used to obtain yttrium and fluoride doped HAs. Five different compositions of doped HAs were prepared. Yttrium amount was kept constant at 2.5 mole %, while fluoride amount was increased from 1 % mole percent to 2.5, 5 and 10 mole %. Descriptions of pure and doped HA samples according to their yttrium and fluoride compositions are summarized in Table 2.1.

Table 2.1. Description and compositions of pure and doped HAs.

Sample ID	**Mole % Y^{3+}**	**Mole % F^-**
HA	0	0
HA2.5Y	2.5	0
HA2.5Y1F	2.5	1
HA2.5Y2.5F	2.5	2.5
HA2.5Y5F	2.5	5
HA2.5Y10F	2.5	10

The amounts of the main precursors were decreased to adjust percentage of the substitutions. The changes in the moles of the main precursors are seen in Table 2.2.

The synthesis procedure was the same as the procedure for pure HA synthesis. Yttrium nitrate was added into the calcium nitrate tetra hydrate solution and ammonium fluoride was added into the di-ammonium hydrogen phosphate solution. After the two solutions were mixed with the same procedure, the final mixture was stirred, aged for two days, filtered, dried at 200°C and sintered at 1100°C for one hour.

Table 2.2. Moles of the precursors used for the synthesis of pure and doped HAs.

Sample ID	**$Ca(NO_3)_2 \cdot 4H_2O$ (mole)**	**$(NH_4)_2HPO_4$ (mole)**	**$Y(NO_3)_3 \cdot 6H_2O$ (mole)**	**NH_4F (mole)**
HA	0.075	0.045	0	0
HA2.5Y	0.073	0.045	0.0019	0
HA2.5Y1F	0.073	0.045	0.0019	0.00075
HA2.5Y2.5F	0.073	0.045	0.0019	0.0019
HA2.5Y5F	0.073	0.045	0.0019	0.0038
HA2.5Y10F	0.073	0.045	0.0019	0.0075

2.2.1.3 Preparation of Pure and Doped HA Discs

After drying the samples at 200°C, they were crushed into powder form with the help of a mortar and pestle. The powders were calcined at 600°C and cold

pressed into a die of 13mm in diameter at 330 MPa for 60 seconds. The obtained discs were then sintered at 1100°C for 1 hour.

2.2.2 Characterization Methods

2.2.2.1 Structural Analysis

2.2.2.1.1 Density Measurement

Densities of the sintered materials were determined by Archimedes method, according to the formula [51]:

$$\rho = m / V \quad (2.1)$$

where: m= weight (gr) ; ρ = density (gr/cm^3); V= disc volume (cm^3).

According to this method, first the dry weights of the materials were measured in order to obtain m. Then weights of the materials in water were measured. The difference between the dry weights and weights of the samples in water gave the volume of the discs. Densities of the materials were thus calculated by the following formula:

$$\rho = \text{dry weight} / (\text{dry weight} - \text{weight in water}) \quad (2.2)$$

Relative densities of the materials were then calculated by comparing the measured densities with the theoretical density of pure HA, which is 3.156 g/cm^3.

2.2.2.1.2 X- Ray Diffraction Analysis

The samples were investigated by X-ray diffraction (XRD) method using a Rigaku DMAX 2200 machine to determine the phases present. XRD was performed on the samples with a Cu-Kα radiation at 40 kV/ 40 mA with a scanning angle from 20^o to 70^o in 2θ with a scan speed of 2.0^o/min. Joint Committee on Powder Diffraction Standards (JCPDS) files were used for comparing the positions of the diffracted planes obtained from the XRD results.

2.2.2.1.2.1 Lattice Parameters of Pure and Doped HA

Unit lattice structure of HA is hexagonal. The hexagonal lattice parameters "a" and "c" of the pure and doped samples were calculated by using successive approximations.

For the calculation "a" of HA, the following formula which is based on Bragg's equation was used. [52]:

$$a_0 = (\frac{\lambda}{2\sin\theta})\sqrt{(\frac{4}{3}(h^2 + hk + k^2) + (\frac{a}{c})^2 l^2)} \quad (2.3)$$

where:

a_0: the calculated lattice constant; λ: x-ray wavelength; θ: the Bragg angle for corresponding (hkl); a/c: the last calculated ratio in successive approximation.

This formula was used to calculate a_0 when the value of the term "$\frac{4}{3}(h^2 + hk + k^2)$" was larger than the value of the term "$(\frac{a}{c})^2 l^2$" for a reflection of (hkl). It was used to calculate c_0 if the value of the term "$h^2 + hk + k^2$" was less

than the value of "l^2". In order to minimize the error caused by incorrect axial ratio, another formula was used for the calculation of c_0 [52]:

$$c_0 = (\frac{\lambda}{2\sin\theta})\sqrt{(\frac{4}{3}(\frac{c}{a})^2(h^2 + hk + k^2) + l^2)} \quad (2.4)$$

The following formula was used to calculate the hexagonal unit cell volume of the materials:

$$V = 2.589(a^2)c \quad (2.5)$$

2.2.2.1.3 Scanning Electron Microscopy Analysis

The samples were polished on papers with grids from 240 to 1200 before examination. Before polishing, sintered samples were embedded in epoxy molds for easy handling. Final polishing was applied with 1μm monocrystalline diamond suspension (Buehler Ltd., USA). Grain size and morphology of the prepared samples were investigated by SEM (QUANTA 400F Field Emission) at a voltage of 20 kV. Prior to the SEM analysis, the samples were coated with gold and platinum under vacuum.

2.2.2.1.3.1 Grain Size Determination

SEM images of the sintered pure and doped HAs were used for grain size determination of the samples. The grain sizes of the samples were determined by the intercept method with a 20 cm circumference circle with the use of the following formula [53]:

$$G_{av} = \frac{L}{N * M} \quad (2.6)$$

where:

G_{av}: average grain size; L: circumference of the circle (20 cm); N: number of intersections along circumference line, M: magnification.

2.2.2.1.4 Fourier Transform Infrared Spectroscopy

In order to determine the presence of OH^- and F^- bonds formed in the structure of pure and doped HAs, FTIR spectra were used. The samples were first crushed into the powder form with the use of mortar and pestle. Ceramic powders were mixed with potassium bromide (KBr) with a weight ratio of 1 to 300. The obtained powder mixture was then cold pressed in order to obtain transparent pellets. The spectra were performed from 1400 cm^{-1} to 400 cm^{-1} with a 512 scan on FTIR spectrometer (Brukers IFS 66/S; Bruker Optics, Germany).

2.2.2.2 Mechanical Testing

2.2.2.2.1 Vickers Micro - Hardness

Micro-hardness test was applied to the samples by a Vickers micro-hardness tester (HMV-2, Shimadzu, Japan). The sintered samples, which were embedded into epoxy molds, were used to determine the micro-hardness of the materials. The molds were polished in order to obtain a flat surface. A load of 200 g was applied by a diamond indenter for 20 seconds onto the surface of the samples. The micro-hardness values of the samples were determined by measuring the length of the

diagonal indent shape, which was formed after the indentation. 20 measurements were performed on each sample. The formula used for the calculation is as follows:

$$HV = 0.001854\frac{P}{d^2} \tag{2.8}$$

where;

HV: Vickers hardness (GPa); P: Applied load (N); d: diagonal indent length (mm).

2.2.2.3 Cell Culture Studies

2.2.2.3.1 Cell Proliferation

For the cell attachment and proliferation tests, Saos-2 cells were seeded on pure and doped HA discs sintered at 1100°C for 1 hr. The discs were sterilized at 200°C for 2 hr prior to seeding. The Saos-2 cells were grown in Dulbecco's modified Eagle medium (DMEM) high glucose supplemented with 10 % fetal bovine serum (FBS) and 0.3 % penicillin-streptomycin. The initial cell seeding density was $5x10^4$ cells/disc. The cells were incubated on HA discs for three different time periods: 3, 7 and 14 days in a carbondioxide incubator (5215, Shel Lab., USA) at 37°C under 5% CO_2 humidified environment. The medium was refreshed every 3 days.

Proliferation of the cells on the discs was analyzed by Methylthiazolyldiphenyl-tetrazolium (MTT) assay. At the end of each time period, the discs were incubated with MTT at 37°C and 5% CO_2 for 4 hours. During

incubation, MTT was reduced into intensely colored formazan, as a result of the enzymatic activity of viable cells. After the discs were rinsed with phosphate buffer saline (PBS), insoluble formazan crystals inside the cells were solubilized and liberated by dimethyl sulfoxide (DMSO) [54]. The absorbance was measured by a μOuant^{TM} microplate spectrophotometer (Biotek Instruments Inc, USA).

2.2.2.3.2 Morphology of the Cells

The morphology of Saos-2 cells seeded on HA discs with a seeding density of 10^5 cells/disc was analyzed by SEM (Quanta 200 FEG, The Netherlands) after 1 and 5 days. After incubation, the medium was removed and cells were fixed with 2.5 % glutaraldehyde in PBS for 2 hours. Following fixation, the cells were rinsed with cacodylite buffer (0.1 M pH: 7.4) and dehydrated with increasing ethanol-water solution series (70, 80, 90 and 100 %). The discs were then immersed in hexamethyldisilazane (HMDS) and dried in air in laminar flow [48]. Prior to SEM examination, the discs were coated with gold by a precision etching coating system (PECS) (Gatan 682, USA) at a thickness of 10nm.

2.2.2.3.3 Alkaline Phosphatase (ALP) Assay

Saos-2 cells were seeded on HA discs with a seeding density of $4x10^4$ cells/disc and incubated for 7 and 14 days. The cells were incubated in osteogenic differentiation medium (DMEM supplemented with 10 % FBS, 1 % penicillin-

streptomycin, 50 µg/ml ascorbic acid, 10 mM β-glycerophosphate and 10^{-8} M dexamethasone), which was refreshed every 3 days.

At the end of each incubation period, the cells on the discs were lysed with 600 µl of 0.1% Triton X-100 containing 0.1 % w/v sodium azide and 1% protease inhibitor in PBS on ice. The cells were kept on ice for 30 minutes and then thawed. The obtained lysates were diluted with osteogenic differentiation medium. 20 µl of each lysate-medium solution was added into 100 µl *p*-nitrophenyl phosphate (pNPP) substrate solution and incubated at 37°C for 30 minutes. During incubation, pNPP was expected to be converted into *p*-nitrophenol and an inorganic phosphate as a result of the intracellular ALP enzyme activity according to the following reaction [55]:

p-nitrophenyl phosphate ⟶ *p*-nitrophenol + phosphate (2.9)

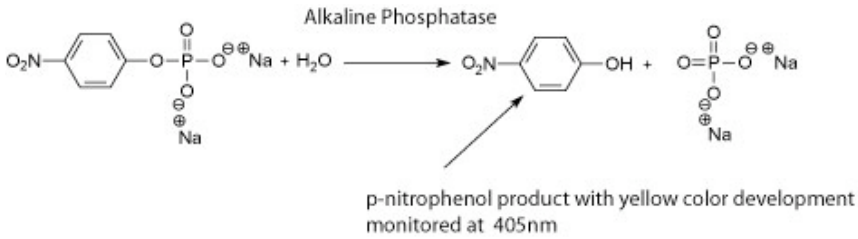

Figure 2.1. Conversion of pNPP into *p*-nitrophenol and an inorganic phosphate [55].

At the end of 30 minutes, the absorbance of each lysate was read at 405 nm by using µOuant™ microplate spectrophotometer. The formed *p*-nitrophenol was determined according to the calibration curve constructed in the range of 25-250

μM (Figure A.1 in Appendix A). ALP activity of each lysate was normalized by its protein content. The specific ALP activity was stated as nmol/μg protein/min.

For determining the protein contents of the lysates, bicinchoninic acid (BCA) assay was used [56]. For this procedure, the substrate solution was prepared by mixing 1ml of copper sulfate solution (2 g cupric sulfate in 50 ml water) with 50 ml of BCA reagent. 50 μl of each cell lysate was added into 1 ml of copper sulfate-BCA mixture and the absorbance was read at 562 nm with a μOuant^{TM} microplate spectrophotometer after 30 minutes of incubation. The protein content of each cell lysate was determined according to the calibration curve obtained with bovine serum albumin (BSA) in the range of 0-1.2 mg/ml (Figure B.1 in Appendix B).

2.2.2.3.4 Dissolution Behavior

Dissolution behavior of pure and doped HA discs in physiological environment was analyzed in DMEM. After sterilization, the HA discs were soaked DMEM [57] and incubated at 37°C in carbondioxide incubator for three different time periods: 1, 7 and 14 days. The volume of DMEM to be used was determined according to the formula:

$$V_s = S_a/10 \tag{2.10}$$

where V_s is the volume of DMEM in ml and S_a is the surface area of a disc in mm^2 [58]. At the end of each incubation period, the discs were removed from the DMEM

solutions and the amount of calcium deposition in the solutions was analyzed by calcium o-cresolphthalein complexone method [59, 60].

A color reagent was prepared by dissolving of 25 mg o-cresolphthalein complexone powder into 250 ml distilled water and with the addition of 15 ml concentric HCl. The buffer was prepared by mixing 37.8 ml adenosine monophosphate (AMP) reagent with 250 ml distilled at a pH of 10.7. 100 µl samples from DMEM solutions were added into 1 ml color reagent and 1 ml buffer. Prepared aliquots were incubated at room temperature on orbital shaker for 15 minutes. Their absorbances at 540 nm were measured by using a µOuant™ microplate spectrophotometer (Biotek Instruments Inc, USA). Calcium amount in the solutions was determined by the calibration curve constructed in the range of 0-12.5 mg/dl (Figure C.1 in Appendix C).

CHAPTER 3

3. RESULTS AND DISCUSSION

3.1 Structural Analysis

3.1.1 Density of the Samples

Densities of the sintered materials and their relative densities compared to theoretical density after the sintering at 1100°C for one hour are shown in Table 3.1.

Table 3.1. Sintered densities and relative densities of pure and doped HAs.

Sample ID	Sintered Density (g/cm^3)	Relative Density (%)
HAP	3	95.1
HA2.5Y	3.03	96.0
HA2.5Y1F	2.95	93.5
HA2.5Y2.5F	2.575	81.6
HA2.5Y5F	2.696	85.4
HA2.5Y10F	2.395	75.9

It was observed that increased F^- ion incorporation lead to a decrease in the density of samples. This result is in agreement with a former study, in which with

the addition of F^- ion, less dense materials were obtained [61]. It was stated that the bond that forms between F^- and OH^- groups decreased the rate of diffusion that regulates the densification [61]. Thus with increasing F^- ion substitution, densification of HA decreased, resulting in less compact structures as observed in the present study.

In literature there are a few mechanisms explaining the density change in HA due to the incorporation of Y^{3+} ions. Ergun et al. reported that Y^{3+} ion substitution led to an increase in the density up to a certain Y^{3+} ion incorporation amount. However, as the amount of Y^{3+} ion substitution increased further, lower densities were obtained [42]. It was reported that the excessive positive charge formed due to the substitution of trivalent Y^{3+} ion for a Ca^{2+} ion is compensated by the formation of a Ca^{2+} ion vacancy for each two Y^{3+} ion substitutions and these vacancies may result in the formation of porosities, which explains the observed lower density with increasing Y^{3+} ion content in that study. In another study, it was proposed that the excessive positive charge formed due to Y^{3+} ion substitution is compensated by an increase in the negative charge via transformation of OH^- ions into O^{2-} ions and obtaining a material with the formula $Ca_{10-x}Y_x(P0_4)_6(OH)_{2-x}O_x$ [62].

There are two possible sites for doping ions to substitute for Ca: Ca (I) and Ca (II). In pure HA, four of the ten calcium atoms occupy Ca (I) position two at level z=0 and two at z=0.5. The remaining six calcium atoms occupy the Ca (II) position, three at z=0.25 and three at z=0.75, surrounding the OH groups located at the corners of the unit cell [30]. The charge balance mechanisms discussed above

for the substitution of trivalent Y^{3+} ion into HA also determines the distribution of Y^{3+} ion between these two sites of calcium [59-66]. It was stated that the rare earth ions and ions with smaller ionic radii than Ca^{2+} ion occupy the Ca (I) site [65, 66]. Thus it can be deduced that Y^{3+} ions substitute for Ca (I) site.

In the present study, it was observed that Y^{3+} ion doping resulted in increased density. In addition to the density results, it was observed by the SEM examinations that, only Y^{3+} doped sample (HA2.5Y) exhibits a less porous structure compared to pure HA (Figure 3.7). Thus it can be concluded that rather than resulting in the formation of vacancies, Y^{3+} doping leads to formation of a more compact structure in the present study and this result can be linked to the case presented in the study of Yamashita et al. [62].

3.1.2 XRD Analysis

XRD patterns of each sintered sample are shown in comparison to standard patterns of HA, α-TCP and β-TCP in Figure 3.1.

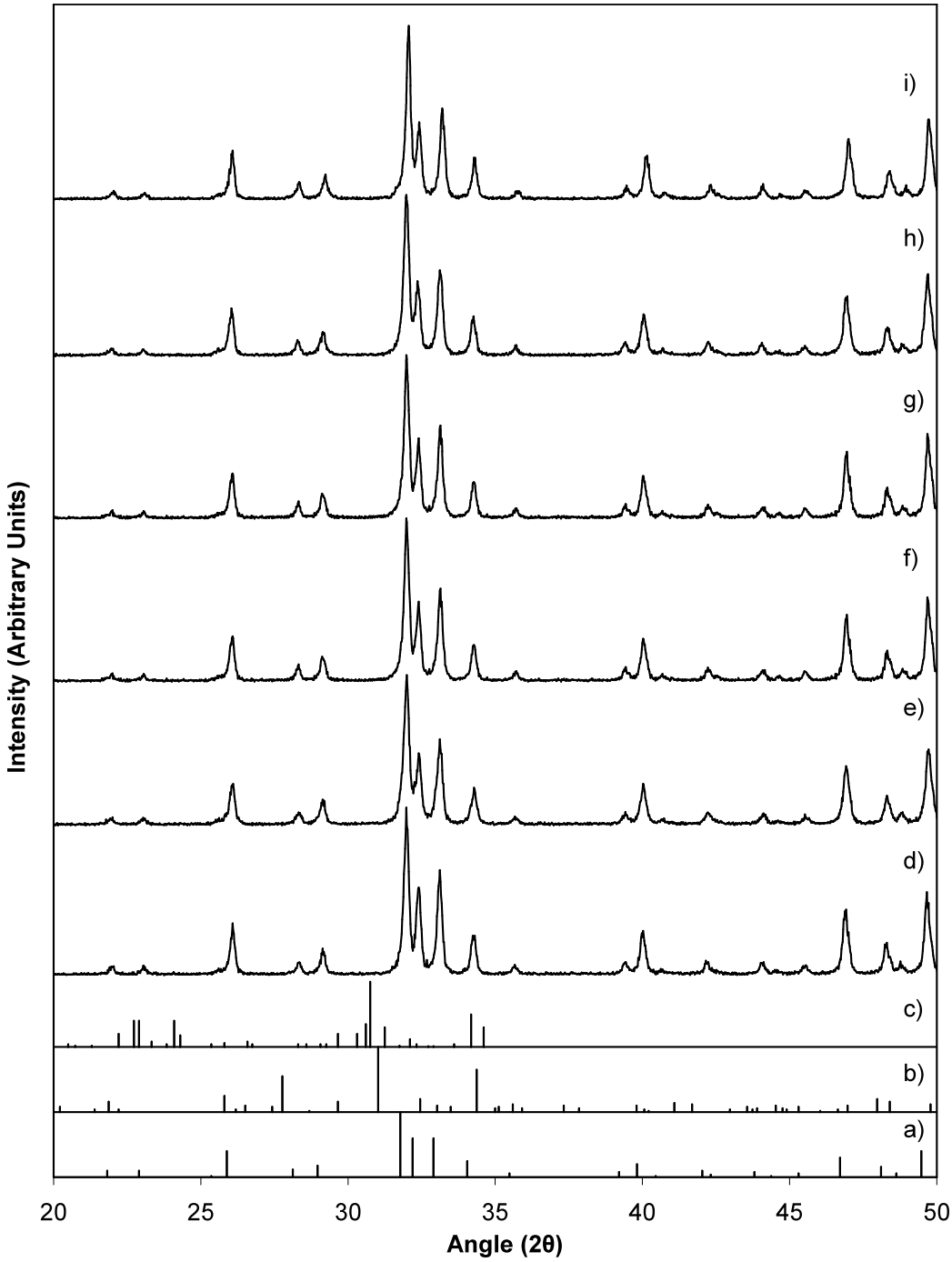

Figure 3.1. XRD patterns of a) Standard HA (JCPDS#: 9-432); b) Standard β-TCP (JCPDS#: 9-169); c) Standard α-TCP (JCPDS#: 9-348); d) HA; e) HA2.5Y, f) HA2.5Y1F, g) HA2.5Y2.5F, h) HA2.5Y5F, i) HA2.5Y10F sintered at 1100°C.

XRD patterns of all the samples were found to match with the Joint Committee on Powder Diffraction Standards (JCPDS) file # 9-432 for HA. There were no secondary phases observed in the XRD patterns of the samples. However, it was previously reported that β-TCP phase was observed in HA sintered at 1100°C for four hours [67]. This may be explained such that; as the sintering time increases, the necessary incubation time for the nucleation and growth of the secondary phases is reached thus their formation becomes easier [68]. It was also reported that β-TCP phase was observed in HA after the sintering at 1300°C [36]. These results indicate that the stability of HA decreases as the sintering time is extended and the sintering temperature is increased. The reason for no secondary phase formation in this study was mainly due to the relatively short sintering time and low sintering temperature. The other probable explanation might be the structural stability provided by precipitation method [27], or the improved structural stability caused by the addition of F^- ion for the doped samples [69]. It was also reported that as the Ca/P ratio of HA approaches to 1.67, the material becomes more stable after sintering [16]. This explains the structural stability of HA in the current study, which has a chemical formula close to that of stoichiometric HA.

Addition of Y^{+3} and F^- ions were not found to cause any severe fluctuations in XRD patterns of the samples except for little shifts from the pattern of pure HA. For example, when the pure and doped samples are compared, the most intense peak which was observed at $2\theta = 31.98$ for HA, was seen at $2\theta = 32$ for HA2.5Y and $2\theta = 32.05$ for HA2.5Y10F (Figure 3.2). These small shifts might be due to the incorporation of doping ions into the unit cell structure of HA.

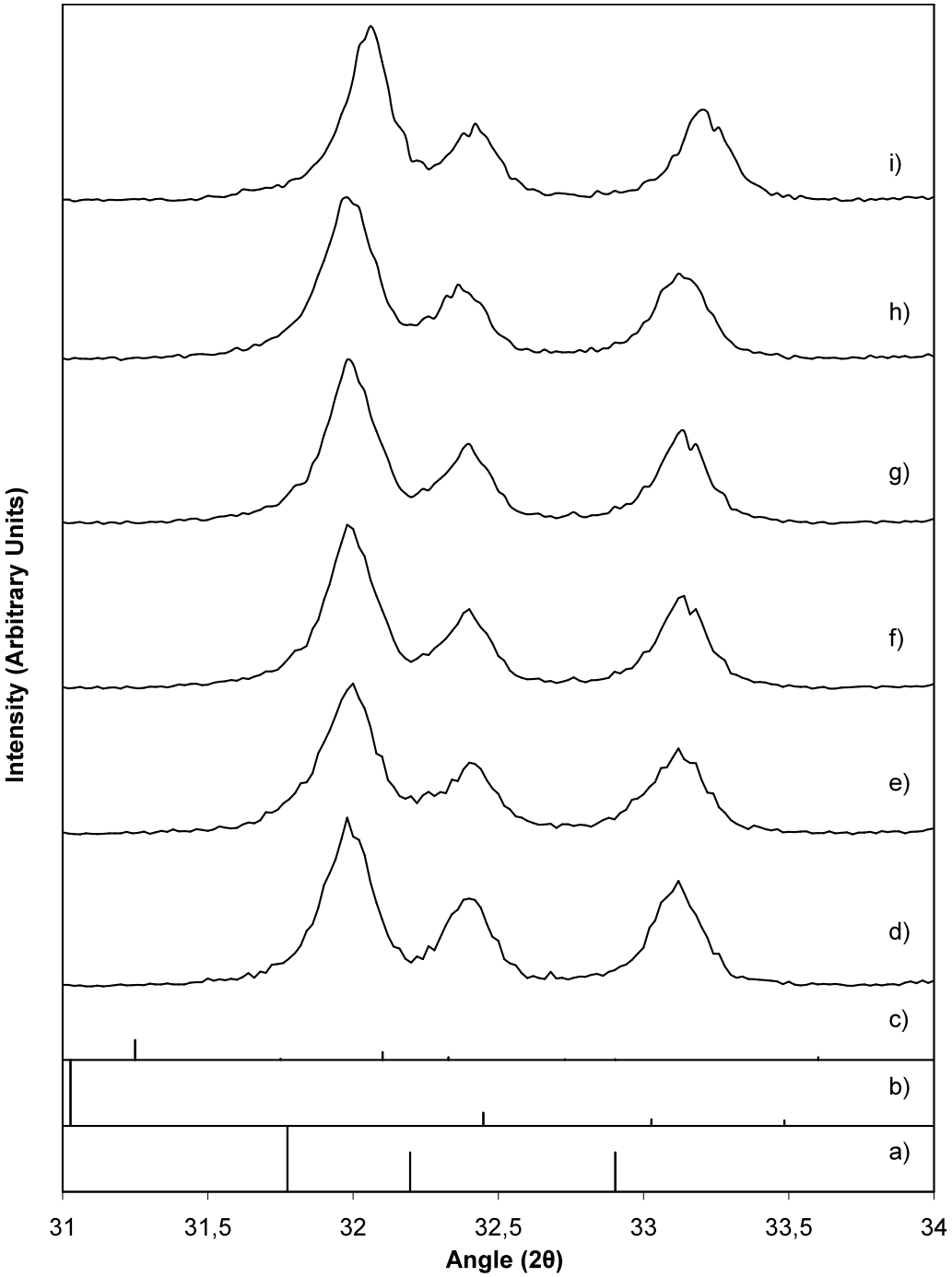

Figure 3.2. XRD patterns of a) Standard HA (JCPDS#: 9-432); b) Standard β-TCP (JCPDS#: 9-169); c) Standard α-TCP (JCPDS#: 9-348); d) HA; e) HA2.5Y, f) HA2.5Y1F, g) HA2.5Y2.5F, h) HA2.5Y5F, i) HA2.5Y10F sintered at 1100°C between the 2Θ range 31-34.

It has also been observed that the intensity of the peaks increased with F^- ion doping. For instance, the intensity of the most intense peak reached to 1287 for HA while this value reached to 1358 for HA2.5Y1F. This might indicate an improvement in the crystallinity of the samples, which was expected since F^- ion incorporation results in an increase in crystallinity [30]. Among the F^- ion doped samples, HA2.5Y1F exhibited relatively higher intensity compared to the others, indicating that HA2.5Y1F had the highest crystallinity.

3.1.2.1 Lattice Parameters of Pure and Doped HAs

In Table 3.2, lattice parameters of pure and doped HAs, changes in lattice parameters a and c, and volumes of the samples with respect to pure HA are presented.

Table 3.2. Hexagonal lattice parameters, unit cell volumes and changes in these values for HA, HA2.5Y, HA2.5Y1F, HA2.5Y2.5F, HA2.5Y5F, HA2.5Y10F.

Sample ID	a (Å)	c (Å)	Δa (Å)	Δc (Å)	V (Å^3)	ΔV (Å^3)
HA	9.3810	6.8557	0.0000	0.0000	1562.0	0.0
HA2.5Y	9.3771	6.8481	-0.0039	-0.0076	1559.0	-3.0
HA2.5Y1F	9.3778	6.8510	-0.0032	-0.0047	1559.9	-2.1
HA2.5Y2.5F	9.3744	6.8484	-0.0066	-0.0073	1558.1	-3.9
HA2.5Y5F	9.3740	6.8580	-0.0070	0.0023	1560.2	-1.8
HA2.5Y10F	9.3546	6.8519	-0.0264	-0.0038	1552.4	-9.6

It was observed that Y^{3+} ion substitution resulted in a decrease in lattice parameters in both a and c directions and the unit cell volume. This result can be explained by the differences in the ionic radii of Ca^{2+} ion (0.99 Å) and Y^{+3} ion (0.90 Å), which substitutes for Ca^{2+} [42]. Since Y^{3+} ion is smaller than Ca^{2+} ion, the shrinkage in lattice parameters and unit cell volume due to Y^{3+} doping is reasonable. This result is in agreement with references [41, 42].

It was reported that substitution of other cations with smaller radii than Ca^{2+} ion such as Cd^{2+}, Mg^{2+}, Zn^{2+}, In^{3+} resulted in a reduction in lattice parameters while addition of cations with larger ionic radii such as Bi^{3+}, La^{3+} lead to an increase in lattice parameters due to the differences in their ionic radii [30, 41, 42]. When ions with higher ionic radii differences are substituted into HA, changes can be observed in the crystallinity or structure of HA in addition to lattice parameters. For example the structural incorporation of Sr^{2+} ion for Ca^{2+} was found to cause increase in the lattice parameters and also expansion in the structural size of HA due to the larger ionic radius of Sr^{2+} (1.13 Å) compared to that of Ca^{2+} ion [70]. Due to their larger radius, Sr^{2+} ions substitute for Ca (II) site, causing a distortion in the crystal structure of the material [70]. These results show that there is a high correlation between ionic radii and lattice parameters for ion substitutions.

When the effects of F^- ion substitutions are observed, it was seen that as the amount of F^- ion substitution increased, lattice parameter "a" gradually decreased while fluctuating changes were observed in the decrement pattern of lattice parameter "c". Since OH^- ions lie along the "c" axis at the center of Ca (II) triangles, F^- ion substitutions for OH^- ions take place along the "c" axis [30]. Thus

no severe changes are observed in the "c" axis of the crystal structure. The decrement in lattice parameter "a" with increasing F^- content may be attributed to the higher electronegativity of the F^- ions compared to OH^- ions that they substitute for [61]. The increased electronegativity difference between Ca^{2+} and F^- ions results in greater attraction between them, thus the decrease in the distance between these two ions leads to a decrease in the length of "a" axis.

When the samples HA2.5Y and HA2.5Y1F were compared, a slight increase in the lattice parameters were observed with the substitution of F^- ion, although F^- ion substitution was expected to result in shrinkage. This might be due to the partial replacement of OH^- ions by F^- ions since further decrease in lattice parameters were observed by increasing F^- ion content.

3.1.3 SEM Examinations

SEM images of pure and doped sintered samples are presented in Figure 3.3. As seen in Figure 3.3, ion incorporation in HA structure resulted in changes in grain size and shape. Compared to the microstructure of pure HA, smaller grains were observed in the microstructure of the doped samples. These observations were verified by the grain size measurements.

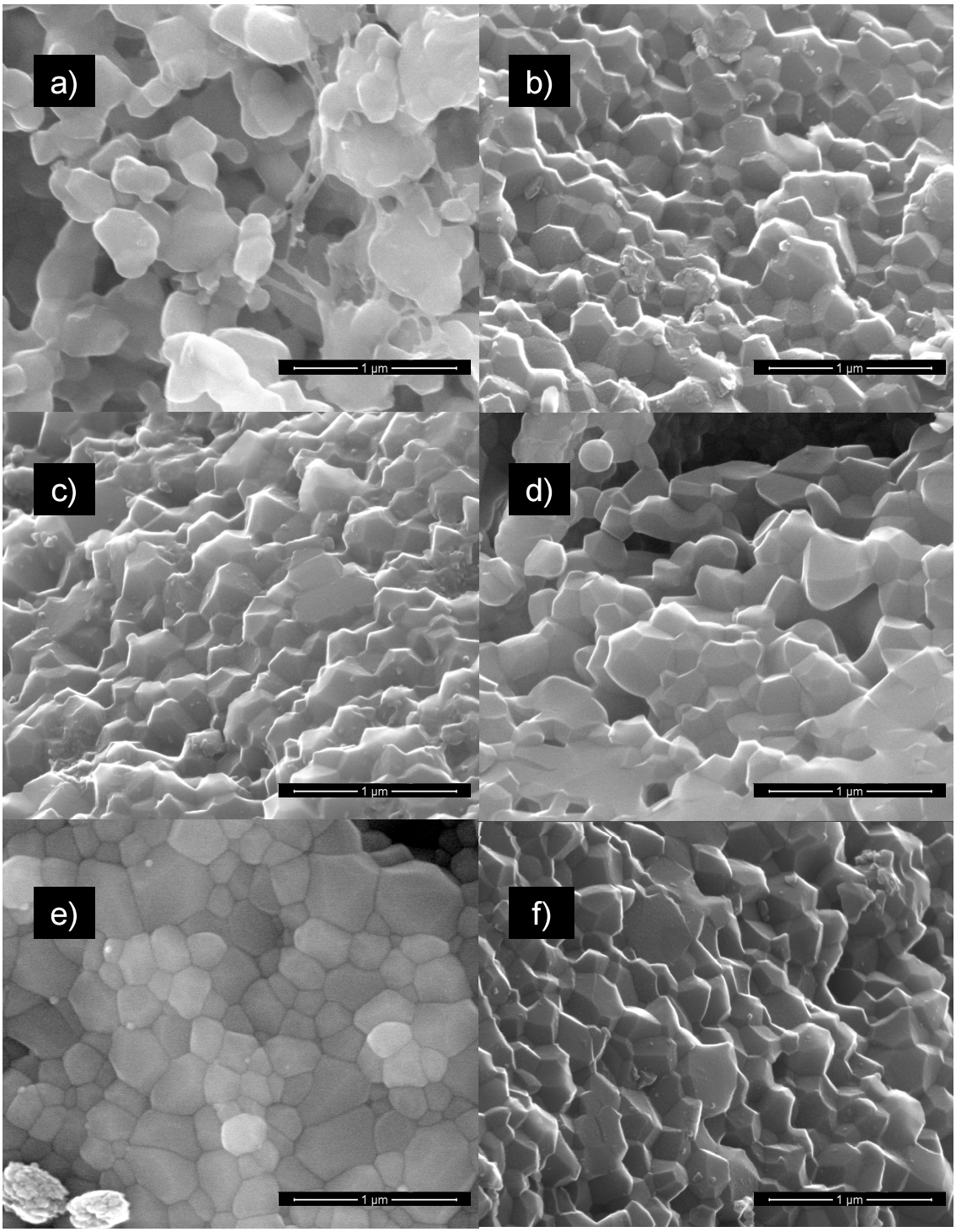

Figure 3.3. SEM images of a) HA; b) HA2.5Y; c) HA2.5Y1F; d) HA2.5Y2.5F; e) HA2.5Y5F; f) HA2.5Y10F.

Grain sizes of pure and doped samples are given in Table 3.3. As seen in Table 3.3, all of the doped samples exhibited smaller grain sizes compared to pure HA. The addition of Y^{3+} ion resulted in a decrease in grain size, which was in consistency with a previous study [42]. Small amounts of F^- ion incorporation resulted in larger grains compared to just Y^{3+} doped samples. However, as the amount of F^- ion increased, average grain sizes of the samples decreased. The bond that forms between F^- and OH^- ions, which lowers densification rate, also decelerates the grain growth thus resulting in smaller grains [61].

The decrease in the lattice parameters due to F^- ion doping was another verification for the decrement in grain sizes.

Table 3.3. Average grain size values of pure and doped HAs.

Sample ID	Average Grain Size (nm)
HA	266
HA2.5Y	159
HA2.5Y1F	208
HA2.5Y2.5F	222
HA2.5Y5F	188
HA2.5Y10F	139

3.1.4 FTIR Analysis

FTIR spectra of pure and doped sintered samples are seen in Figure 3.4. The characteristic peaks of HA were observed for all samples. The assignments and reference frequencies for HA and FHA are given in Table 3.4.

In all the samples, the characteristic peaks showing the vibrations of PO_4^{3-} groups were seen (Figure 3.4). The alterations observed in the spectra due to the incorporation of doping elements are discussed below.

The peak assigned to the OH^- libration band was seen at 630 cm^{-1} for pure HA. For the F^- ion doped samples a gradual decrease in the intensity of the peaks was observed with a shift towards 700 cm^{-1}, which indicated the incorporation of F^- ions for OH^- ions (Figure 3.5).

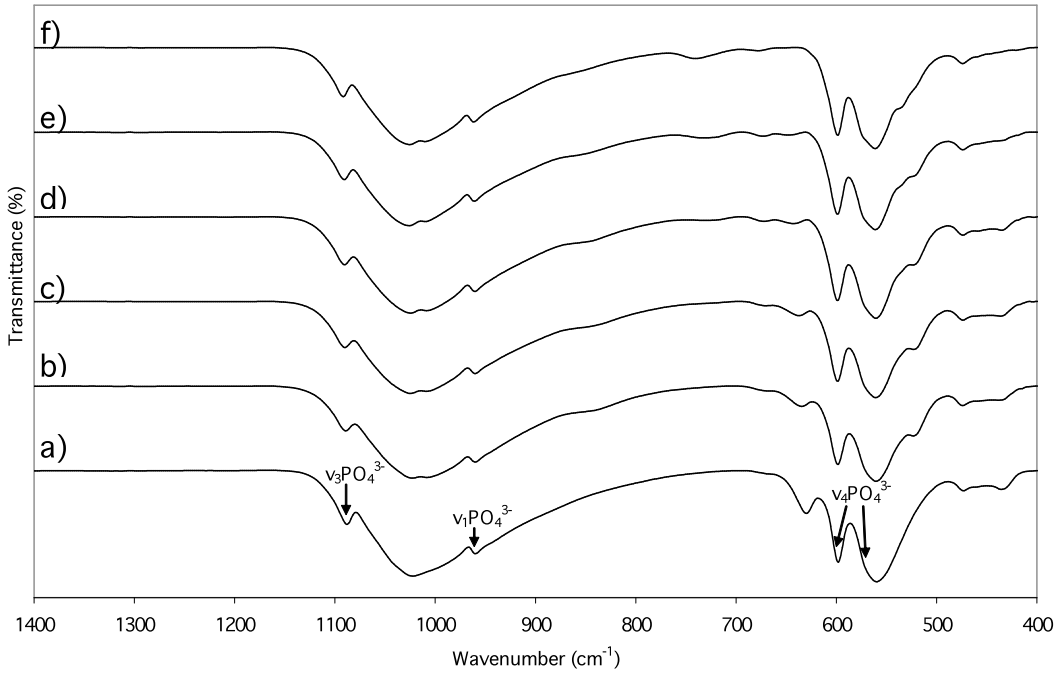

Figure 3.4. FTIR patterns of a) HA; b) HA2.5Y; c) HA2.5Y1F; d) HA2.5Y2.5F; e) HA2.5Y5F; f) HA2.5Y10F in the frequency range of 1400 – 400 cm^{-1}.

Table 3.4. Frequencies (in cm^{-1}) and assignments of bands in FTIR spectra of HA and FHA[47, 69].

Assignment	Apatites (infrared frequency cm^{-1})	
	HA	**FHA**
OH^- (stretching)	3572	-
OH^- (liberational)	630	744
$v_3PO_4^{3-}$ stretch	1046, 1087	1048, 1085
$v_1PO_4^{3-}$ stretch	962	970
$v_4PO_4^{3-}$ bend	571, 601	568, 605
$v_2PO_4^{3-}$ bend	474	473
CO_3^{2-}	1383	779, 1473
OH…F	-	3546

The decrease in the intensity of OH^- libration band was also seen in the sample HA2.5Y, which does not include F^- ions. This result can be explained by the transformation of OH^- ions into O^{2-} ions for the compensation of the excess positive charge that results from the incorporation of trivalent Y^{3+} ion [62]. This result also confirms the explanation for the increase in the density of HA2.5Y in section 3.1.1.

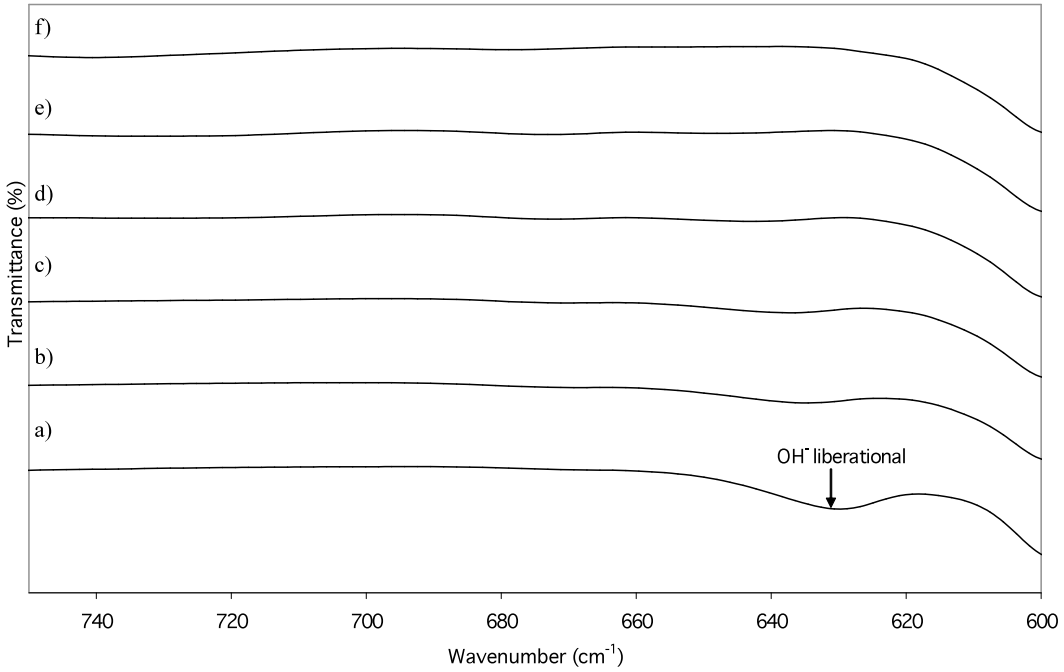

Figure 3.5. FTIR patterns of a) HA; b) HA2.5Y; c) HA2.5Y1F; d) HA2.5Y2.5F; e) HA2.5Y5F; f) HA2.5Y10F in the frequency range of 750-600 cm^{-1}.

Another indication of F^- ion incorporation for OH^- ions was observed in the behavior of the peaks around the frequencies of OH^- stretching (Figure 3.6). It is evidently seen in Figure 3.6 that, as the amount of F^- ion increased, the curve in the vicinity of OH^- stretching band (3570 cm^{-1}) became less and less clear. In the spectra of F^- ion doped samples, a curvature was observed around 3550-3540 cm^{-1} bands, which indicated presence of F^- ions in the structure of HA. These curves also became less and less clear as the amount of F^- ions decreased. These findings prove the substitution of F^- for OH^- ions.

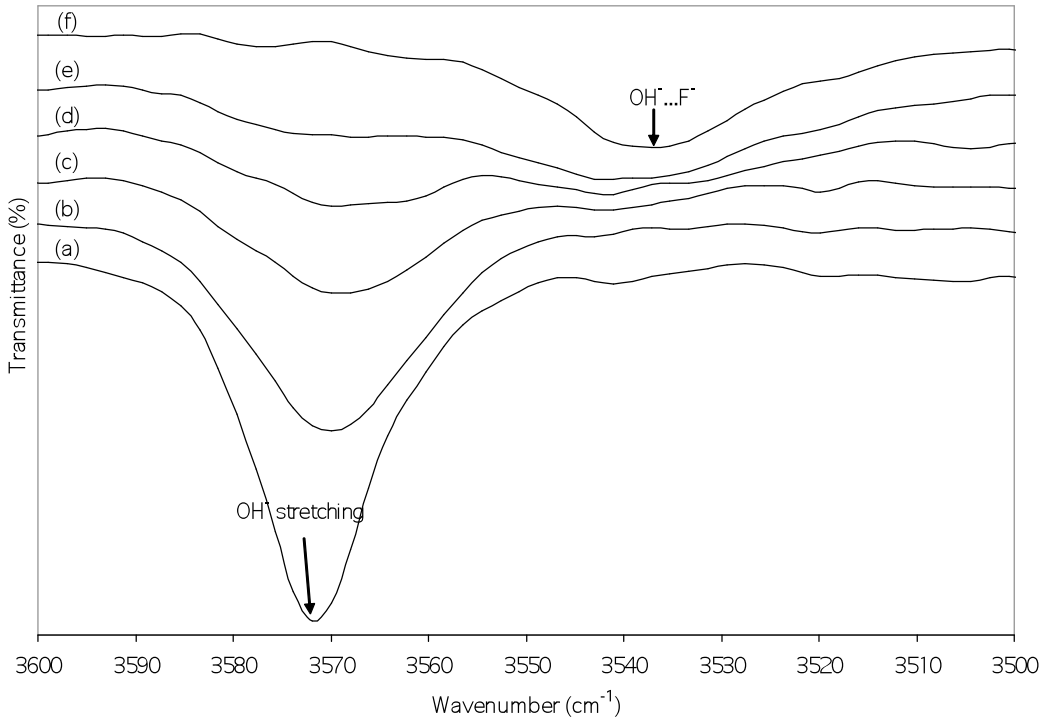

Figure 3.6. FTIR pattern of a) HA; b) HA2.5Y; c) HA2.5Y1F; d) HA2.5Y2.5F; e) HA2.5Y5F; f) HA2.5Y10F in the frequency range of 3600-3500 cm^{-1}.

3.2 Mechanical Tests

3.2.1 Vickers Micro–Hardness Tests

In order to compare the mechanical properties of doped and undoped samples, micro-hardness values of the samples were determined. In Table 3.5, average micro-hardness of each sample are given.

Table 3.5. Average micro-hardness of pure and doped HAs.

Sample ID	Micro-Hardness (GPa)
HA	6.308 ± 0.218
HA2.5Y	6.080 ± 0.220
HA2.5Y1F	6.559 ± 0.241
HA2.5Y2.5F	6.053 ± 0.254
HA2.5Y5F	5.722 ± 0.236
HA2.5Y10F	5.990 ± 0.229

As seen in Table 3.5, micro-hardness values of most of the doped samples are close to micro-hardness of pure HA. The highest increase in micro-hardness among the doped materials was seen in HA2.5Y1F. After this sample, a decrease in microhardness values was observed as the amount of F^- ion increased. This result showed a consistency with the study, which showed that F^- incorporation improved mechanical properties only up to a certain limit [50]. After that limit was exceeded, a decrease in mechanical properties was observed, as in this study. Eslami et al. also agrees that the partial replacement of OH^- ions by F^- ions leads to improvements in mechanical properties and states that during the partial replacement of OH^- ions by F^- ions, hydrogen ions from the former OH^- ions bound to high affinity F^- ions instead of O^{2-} ions, producing a good ordered apatite structure with better mechanical properties [47].

The variations in the microhardness values of the samples depending on the changes in F^- ion content, exhibited a similar pattern with the variations in the

densities of the samples. Among the fluoride doped samples, highest density and highest microhardness values were seen in HA2.5Y1F. Low density values indicated the presence of pores in the structure of materials. Since porous materials exhibit poor mechanical properties compared to dense ones, the impairment of microhardness due to decreasing density is a reasonable result. Similar findings of Gross et al. confirm this result [50].

3.3 Cell Culture Studies

3.3.1 Cell Proliferation

Cell proliferation on pure and doped HA discs sintered at 1100°C was analyzed by MTT viability assay (Figure 3.7). The cell number on all discs increased with culture time.

On day 3, all the doped samples except HA2.5Y1F exhibited slightly lower cell proliferation compared to that of pure HA. The degree of cell proliferation on HA2.5Y1F was the highest among all discs. No statistical difference was observed in cell proliferation among pure and doped HA discs on day 3.

After 7 days of incubation, a small increase in cell number was observed for all samples. There were no statistically significant differences in cell proliferation on discs at day 7 and between the incubation periods day 3 and day 7.

On the 14^{th} day, a sharp increase was observed in the proliferation of the cells, especially with increasing F^- ion doping amounts. Statistical differences were observed in the OD readings of HA2.5Y2.5F, HA2.5Y5F and HA2.5Y10F between

days 3 and 14, indicating that cells significantly increased in number. No statistically significant differences in cell proliferation were observed on discs of different groups at day 14.

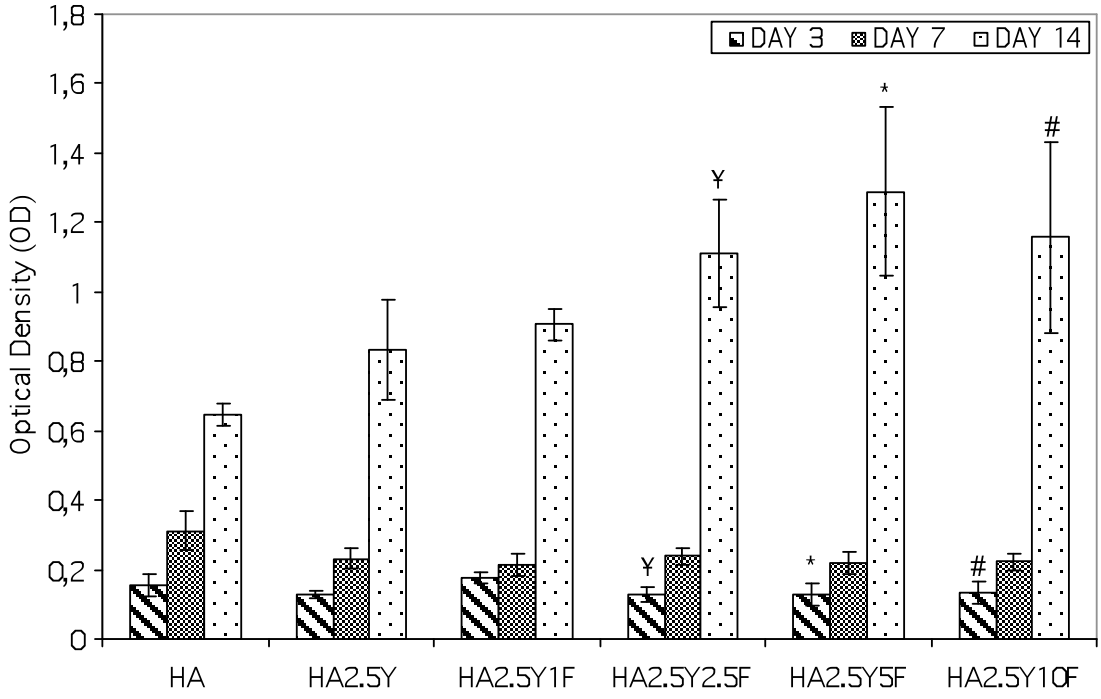

Figure 3.7. Cell proliferation on pure and doped HA discs sintered at 1100°C. (Statistically significant differences between the groups: *, #, ¥ $p \leq 0.05$)

It was observed that incorporation of Y^{3+} and F^- ions do not have any adverse effects on the biocompatibility of HA. Moreover, F^- ion incorporation was found to improve cell proliferation on HA with longer incubation periods. On day 7, F^- ion doped samples exhibited slightly lower OD values compared to those of pure HA. This finding is in agreement with the former studies which reported that OH^- groups provided binding sites for cell attachment and when F^- ions replace OH^- groups, a decrement was observed in the cell attachment and proliferation rates of

HA in the first place [47, 48]. However with incubation, more F^- ions were released into the cell culture medium, stimulating cell attachment and proliferation on HA [47, 48, 71]. This explains the significantly higher cell proliferation observed on F^- ion doped samples on day 14 compared to pure HA and HA2.5Y.

An increasing trend in cell proliferation was observed with increasing F^- ion content up to 5 mole % of F^- ion doping, after which a decrement was observed in cell proliferation. The highest degree of proliferation was observed on HA2.5Y5F after 14 days of incubation, which was in agreement with literature. It was reported that a moderate amount of F^- ion should be added in order to achieve higher proliferation rates [70-72, 74].

Y^{3+} incorporation was also found to have a positive effect on cell proliferation especially at 14 days of incubation (Figure 3.7) as reported previously [36, 45]. It was seen that co-substitution of Y^{3+} and F^- ions resulted in higher cell proliferation. The smaller grain sizes obtained with doping (Table 3.3) might be another contributing factor to enhance cell proliferation since HA with smaller grains sizes was reported to result in improved cell attachment and proliferation [75, 76].

3.3.2 Morphology of the Cells

SEM images of the cells cultured on pure and doped HA discs for 1 and 5 days are presented in Figures 3.8-3.11. It was observed that after 1 day post seeding, cells were attached and they even started to spread on the surfaces of all discs. At lower magnifications, the cells were observed more in the center of HA discs (data

not shown) after 1 day of incubation. The cells were near confluency at the center. This was due to seeding of the cells in a sample volume at the center of the discs (25µl). The number of attached cells was relatively lower on HA2.5Y1F compared to the other doped and pure samples. However, better cell attachment was observed on HA discs with F^- ion content higher than 1%, which was in agreement with MTT results (Figure 3.7).

After 5 days of incubation, the cells were observed to spread on all disc surfaces. Cells were also observed at the periphery of the discs (data not shown), which showed that pure and doped HA discs provided a favorable environment for cell proliferation. This finding was in agreement with cell proliferation results (Figure 3.7). The cell layer formed on the samples exhibited a more compact structure on day 5 compared to day 1. The cells proliferated forming a thick layer, such that material surface could not be observed in most areas (Figures 3.14 and 3.15). HA2.5Y2.5F and HA2.5Y5F especially exhibited very intense layers of cells on day 5, which showed that those doping compositions were relatively more favorable for cell proliferation, parallel in with MTT results.

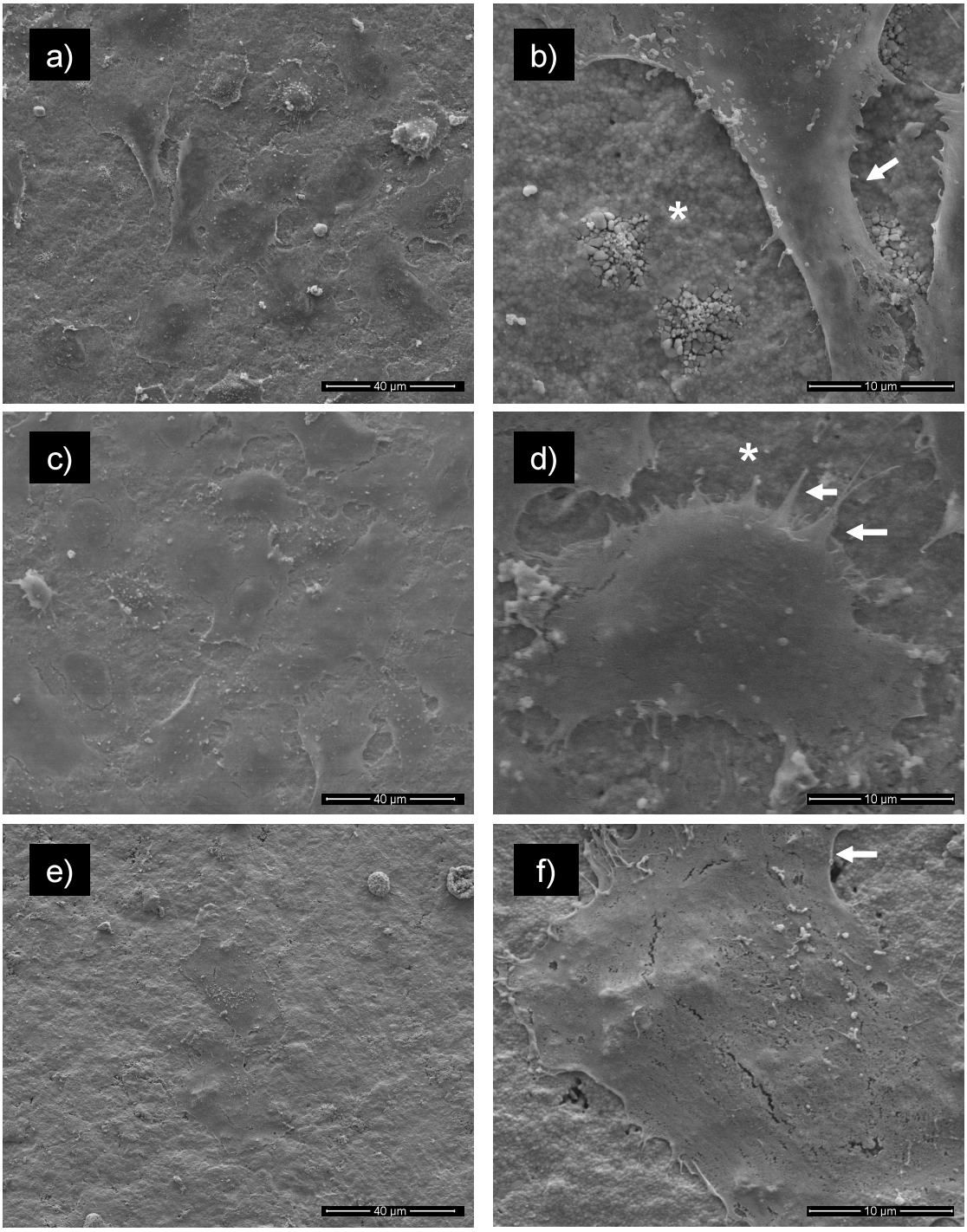

Figure 3.8. SEM images of cells on a and b) HA, c and d) HA2.5Y, e and f) HA2.5Y1F discs (day 1). (* indicates disc surface. Arrows show lamellopodia of the cells.)

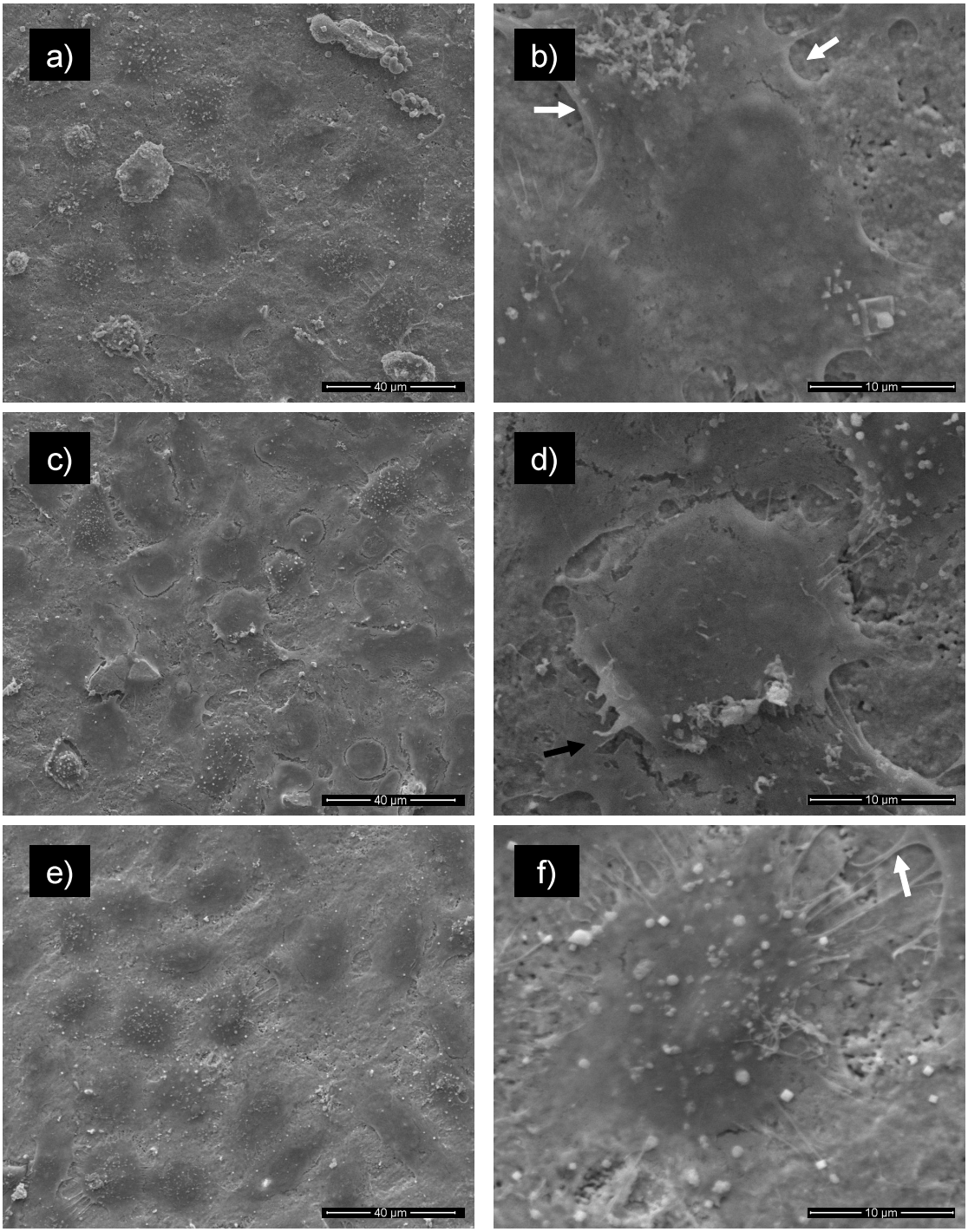

Figure 3.9. SEM images of cells on a and b) HA2.5Y2.5F, c and d) HA2.5Y5F e and f) HA2.5Y10F discs (day 1).

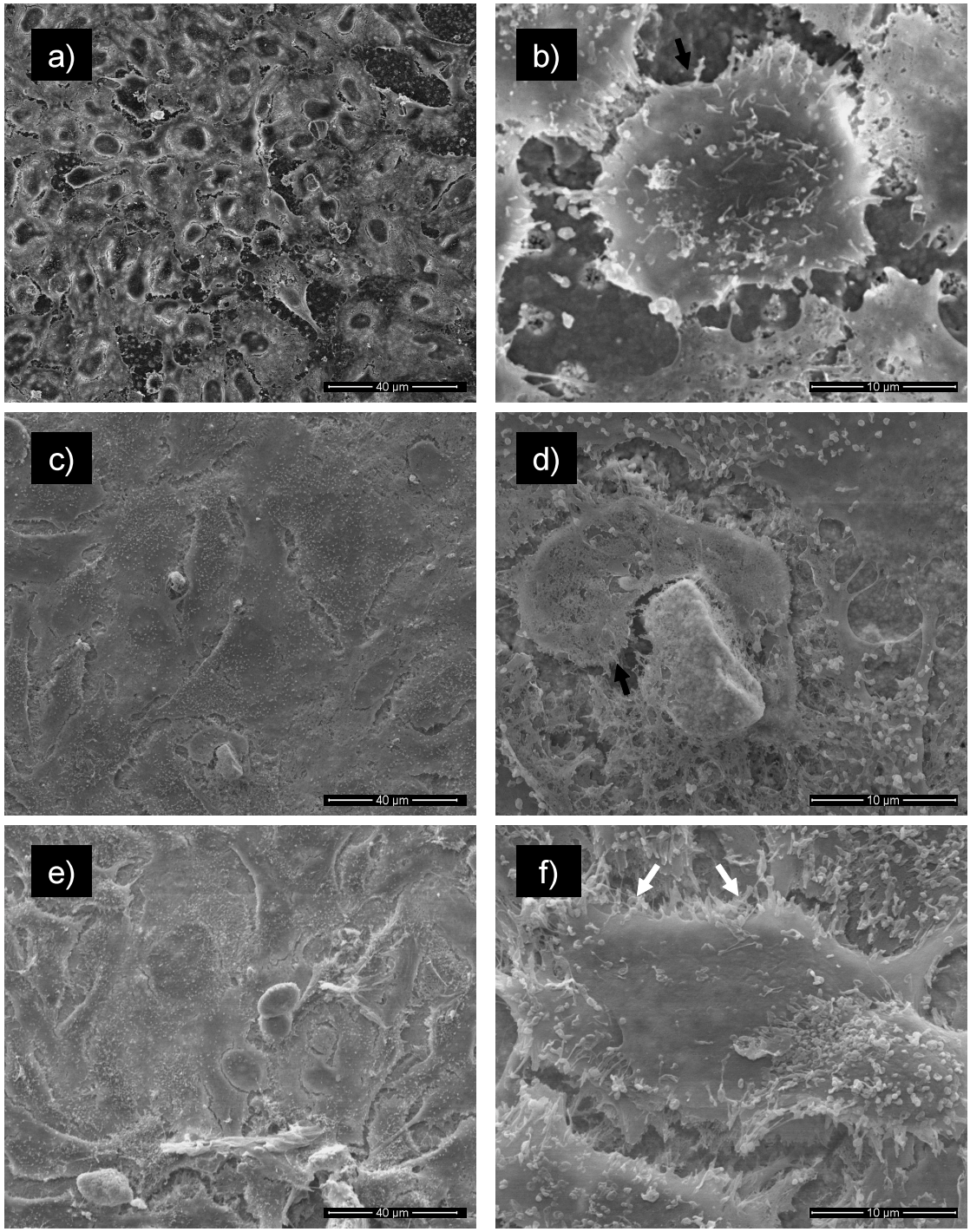

Figure 3.10. SEM images of cells on a and b) HA, c and d) HA2.5Y, e and f) HA2.5Y1F discs (day 5). (Arrows show pseudopodia of cells.)

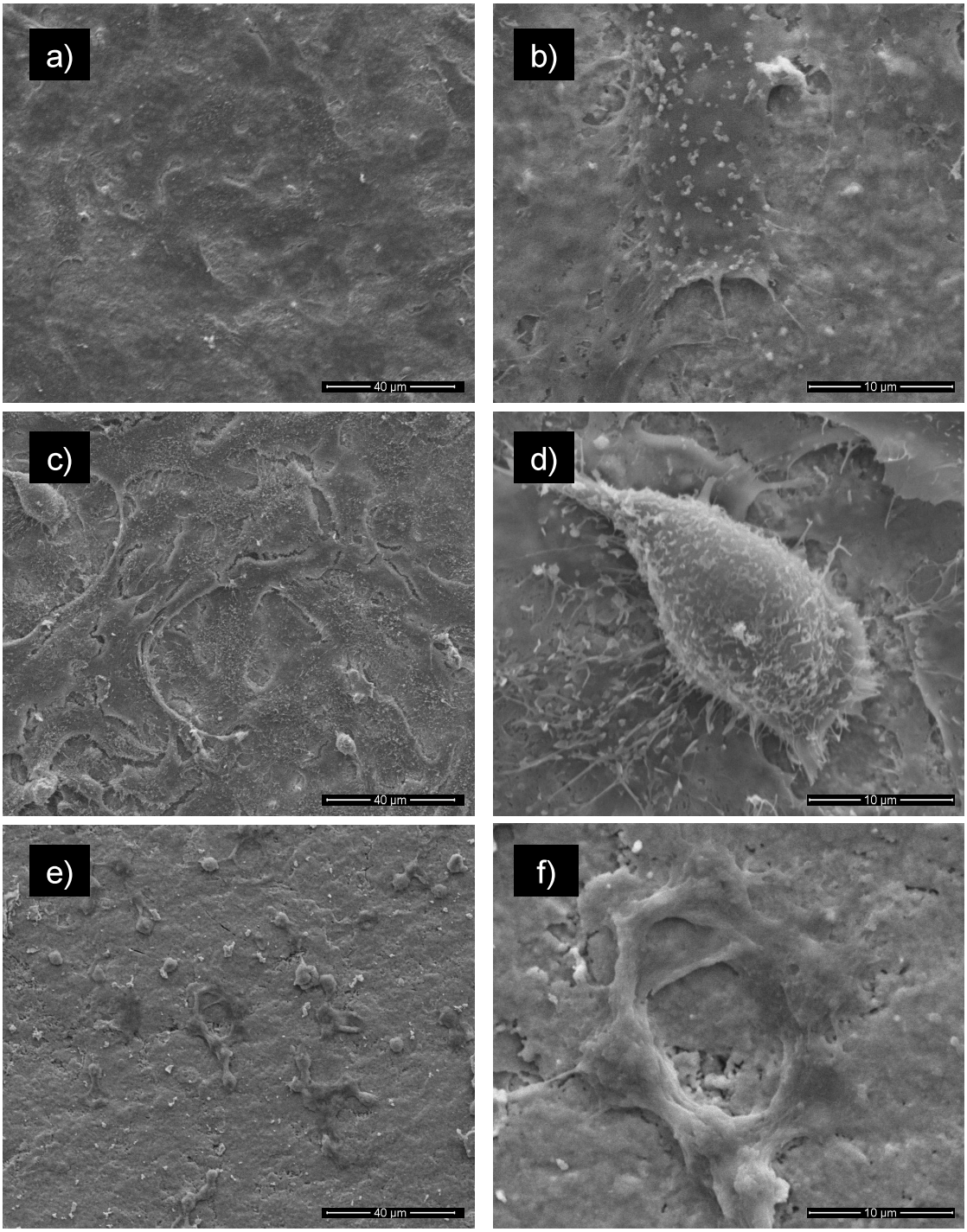

Figure 3.11. SEM images of cells on a and b) HA2.5Y2.5F, c and d) HA2.5Y5F e and f) HA2.5Y10F discs (day 5).

3.3.3 ALP Assay

Osteoblast cells secrete ALP during active bone deposition thus ALP is one of the early markers to bone formation and osteoblastic activity [77]. ALP activities were measured to investigate the effect of Y^{3+} and F^- ion substitution on osteogenic differentiation of Saos-2 cells. In Figure 3.12, ALP activities of the cells on pure and doped HA after 7 and 14 days of incubation are presented.

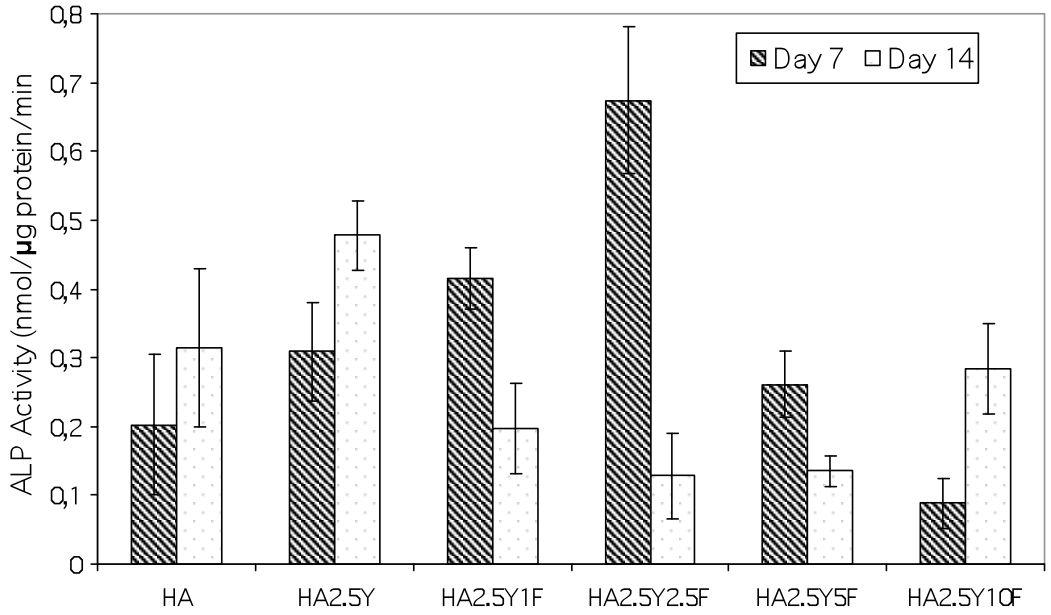

Figure 3.12. ALP Activity of cells on on pure and doped HA discs sintered at 1100°C.

It was observed that the doped samples HA2.5Y, HA2.5Y1F and HA2.5Y2.5F resulted in higher ALP activity compared to pure HA. This result indicated that incorporation of Y^{3+} ion positively affected the differentiation of cells and its effect was improved by the co-substitution of F^- ion up to 2.5 mole% F^- ion content. On day 7, increasing F^- ion content led to an increment in ALP activities up to 2.5 mole % F^-, however with further F^- ion incorporation, lower ALP activities

were obtained. The highest ALP activity was observed for HA2.5Y2.5F on day 7, which was also statistically higher than pure HA on day 7. This result is in agreement with the former studies, in which it was reported that a certain amount of F^- ion was necessary to stimulate early cell differentiation [48, 74, 78, 79].

The ALP activity of the cells on HA2.5Y was improved with time, similar to pure HA. However, for F^- doped samples fluctuations were observed in ALP activities of cells, rather than a remarkable trend depending on the amount of F^- ion content. It was observed that ALP activities decreased for F^- ion doped samples except for HA2.5Y10F. This result might indicate that after reaching a high level of differentiation on day 7, cells on the discs HA2.5Y1F, HA2.5Y2.5F, HA2.5Y5F switched to the next differentiation stage, while the other samples remained on the existing differentiation stage [80]. The relatively high ALP activity of the cells on HA2.5Y1F and HA2.5Y2.5F discs on day 7 might be attributed the dissolution and mineralization behavior of these discs. Different Ca^{2+} and F^- ion releases from the discs with different F^- ion content should be considered as an important parameter affecting the cells differentiation behavior on discs.

Overall it can be concluded that F^- ion substitution has a stimulating effect on the differentiation behavior of the cells and an optimum F^- ion level is necessary for a high differentiation.

3.3.4 Dissolution Behavior

In order to determine the dissolution behavior of pure and doped HA discs in DMEM solution, the discs were incubated for 14 days and the Ca^{2+} ion concentrations in the solutions were analyzed. Ca^{2+} ion concentrations of the DMEM solutions after incubation of discs for 1, 7 and 14 days are compared in Figure 3.13.

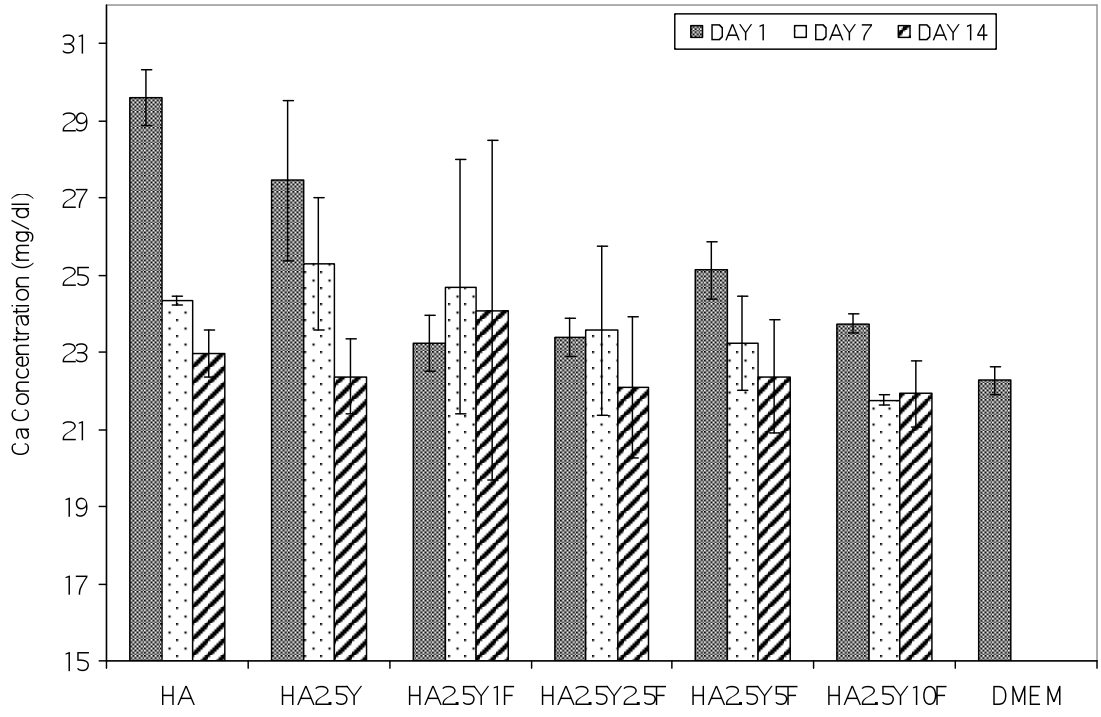

Figure 3.13. Ca^{2+} ion concentrations of the DMEM solutions after 14 days incubation with pure and doped HA discs.

It was observed that Ca^{2+} ion concentrations of all the solutions slightly increased compared to untreated DMEM. This indicates that dissolution of ions occur in the DMEM solutions for all samples. The highest Ca^{2+} ion concentration was observed in DMEM solution of pure HA, indicating this group had the fastest

dissolution. All F^- ion doped discs exhibited lower dissolution rates. This finding is in agreement with previous findings, which state that incorporation of F^- ion into HA improves its chemical stability, thus reduces its solubility [47, 49, 70, 72, 73]. It was reported that during the partial replacement of OH^- ions with F^- ions, the hydrogen atoms of the OH^- ions bound to the new F^- ions with higher affinity, producing a chemically more stable and less soluble material. HA2.5Y1F exhibited the slowest dissolution with the lowest Ca^{2+} ion concentration observed in the DMEM solution of this disc. This result might indicate that, HA2.5Y1F is the most stable material among the F^- ion doped samples. Findings of the XRD analysis also confirm this result (Section 3.1.2)

A rapid decrease in Ca^{2+} ion concentration in DMEM was observed on day 7 for pure HA, HA2.5Y, and HA2.5Y5F discs, which was followed by a relatively slower decrease on day 14. It was previously reported that, following the initial dissolution and Ca^{2+} ion release, a supersaturation state was reached for Ca^{2+} ions in the solution, which favored nucleation [81]. This stimulated the formation of a calcium rich apatite layer on the discs which consumed Ca^{2+} ions. Such Ca^{2+} ion consumption resulted in lower Ca^{2+} ion concentration in the solutions [57, 73, 81]. In agreement with these previous studies, the behavior observed for pure HA, HA2.5Y, and HA2.5Y5F discs might exhibit the signs of formation of an apatite layer on the materials. Moreover, the Ca^{2+} ion concentration reached in the DMEM solutions of these discs was almost equal to that of untreated DMEM, suggesting that equilibrium was reached between the discs and DMEM solutions following apatite formation.

In the solutions with HA2.5Y1F and HA2.5Y2.5F, a different behavior was observed on day 7 and 14. Ca^{2+} ion concentration in DMEM solutions of these discs slightly increased on day 7 compared to that on day 1, suggesting that dissolution continued on day 7. On day 14, Ca^{2+} ion concentration in the DMEM solution of HA2.5Y2.5F decreased and reached that of untreated DMEM. This result might indicate that dissolution was followed by apatite formation on the disc, until equilibrium was reached between this disc and DMEM solution. The Ca^{2+} ion concentration in DMEM solutions of HA2.5Y1F decreased on day 14 compared to day 7, however it did not reach the Ca^{2+} ion concentration of untreated DMEM solution. This result might indicate that apatite formation continued on this sample. This might be attributed to the delayed dissolution and apatite formation behavior of HA2.5Y1F due to its chemically more stable structure.

Ca^{2+} ion concentration of the DMEM with HA2.5Y10F decreased on day 7 and reached the lowest Ca^{2+} ion concentration among all the discs. No significant changes were observed in the Ca^{2+} ion concentration of the DMEM solution with HA2.5Y10F after day 7. This result might suggest that apatite formation stopped and equilibrium was reached in earlier stages for disc compared to the other discs. It was reported that the apatite layer formed on the material surface controls its later dissolution behavior [47, 73]. In F^- ion doped samples, more Ca^{2+} ions are expected to be attracted to the material surface due to increased negative charges, which would result in more apatite formation on the samples with higher fluoridation [49, 73]. The current study is in agreement with these statements such that decreasing

Ca^{2+} ion concentrations were observed with increasing F^- ion content on day 14. These also might explain the dissolution behavior of HA2.5Y10F on day 7 and 14.

It is possible to make some correlations between the cellular activity and dissolution behavior of the samples. Previous studies have reported Ca^{2+} and F^- ion release had a positive effect on cell proliferation [47, 48, 72]. However, it was also stated that high fluoridation rates resulted in lower solubility of HA thus less ion release which would inhibit cell proliferation [47, 48, 54, 70, 73]. In the current study, F^- ion incorporation was observed to positively affect the proliferation of cells on the discs. With increasing F^- ion content, higher proliferation was achieved up to 5 mole % F^- ion incorporation, after which a slightly lower proliferation was observed. The dissolution behavior of fluoridated samples also exhibited a similar pattern such that dissolution rates of the samples increased up to 5 mole % F^- ion incorporation, after which a slightly lower dissolution was observed. These results may indicate that reaching a certain F^- ion content decreased the solubility and limited the ion release of HA, which also reduced proliferation on this sample. This shows that dissolution and F^- ion release plays a role in cell proliferation behavior on the samples in the current study in agreement with Wang et al [72].

On day 7, ALP activity of the cells on HA2.5Y1F, HA2.5Y2.5F, HA2.5Y5F discs and Ca^{2+} ion concentrations of the DMEM solutions of these samples were higher than those of HA2.5Y10F (Figures 3.12 and 3.13). This result is in agreement with the findings of Ma et al [82] in which it was reported that the presence of Ca^{2+} ions in cell culture media enhanced the differentiation of cells. It was also reported that ALP activity was expected to increase just before the

initiation of mineralization [83, 84]. Thus, the decrease in the ALP activities of cells on HA2.5Y1F, HA2.5Y2.5F, HA2.5Y5F discs after reaching the maximum on day 7, might be considered as a sign of mineralization on these discs on day 14 [83, 84].

These results showed the positive effect of F^- ion incorporation on the chemical stability and dissolution properties of HA and that it was possible to tailor the dissolution rate of HA in physiological conditions by varying its F^- ion content.

CHAPTER 4

4. CONCLUSION

In this study, HA was synthesized by a precipitation method and doped with constant amount of Y^{3+} and varying amounts of F^- ions in order to investigate its structural, mechanical and biocompatibility properties. All the samples were sintered at 1100°C for 1 hr.

Y^{3+} doped sample had higher density than pure HA. However, addition of F^- ions resulted in a decrease in density. In XRD patterns, no secondary phase formation was observed upon doping. Small shifts from the XRD peak positions of pure HA and increased peak densities were observed due to the incorporation of doping ions and increased crystallinity. Lattice parameters and unit cell volumes were found to decrease upon substitution of Y^{3+} and F^- ions. These substitutions resulted in smaller grains by SEM analysis. In FTIR spectroscopy analysis, all the doped samples exhibited the characteristic bands of HA. Some additional peaks were observed in the doped samples indicating the successful incorporation of F^- ions. The microhardness values of the samples were found to increase upon addition of F^- ions up to a certain extent, however further increase in F^- ion incorporation led to a decrease in microhardness of the samples.

In cell culture studies, proliferation, morphology and osteogenic differentiation of Saos-2 cells on the sample discs were analyzed. Cell proliferation results revealed that incorporation of Y^{3+} and F^- ions had a positive effect on cell proliferation. Higher proliferation was observed on the discs with increasing fluoridation. SEM investigations showed that the cells attached and proliferated with time on pure and doped HA discs. ALP assays showed that an optimum F^- ion content up to 2.5 mole% was necessary in order to achieve high ALP activity. The dissolution behavior of discs revealed that F^- incorporation increased chemical stability and decreased dissolution rate.

According to the results of structural, microhardness and biocompatibility analysis, HA2.5Y1F was found promising for biomedical applications. This material gave the highest microhardness value, as well as relatively high density, small grain size and low dissolution rate. It also yielded good cell proliferation and differentiation properties. Further investigations are necessary in order to analyze and improve the properties of this material.

REFERENCES

[1] J.Y. Rho, L. Kuhn-Spearing, P. Zioupos, "Mechanical properties and the hierarchical structure of bone", Medical Engineering & Physics 20 (1998) 92-102.

[2] T. Wang, Z. Feng, "Dynamic mechanical properties of cortical bone: The effect of mineral content", Materials Letters 59 (2005) 2277-2280.

[3] N.K. Aras, G. Yilmaz, S. Alkan, F. Korkusuz, "Trace elements in human bone determined by neutron activation analysis", Journal of Radioanalytical and Nuclear Chemistry 239 (1999) 79-86.

[4] R.B. Martin, D.B. Burr, N.A. Sharkey, "Skeletal Tissue Mechanics", Springer (1998) 39-40.

[5] B. Ji, H. Gao, "Mechanical properties of nanostructure of biological materials", Journal of the Mechanics and Physics of Solids 52 (2004) 1963–1990.

[6] M.C. Ho Ba Tho, "Bone and joints modelling with individualized geometric and mechanical properties derived from medical image: Application to the evaluation of osteoarticular pathology", Second MIT Conference on Computational Fluid and Solid Mechanics (2003) 1719-1722

[7] D.M. Cullinane, T.A. Einhorn, "Biomechanics of Bone" Principles of Bone Biology, Second Edition, Volume 1, (2002) 17–32.

[8] B. Ji, H. Gao, "Elastic properties of nanocomposite structure of bone", Composites Science and Technology 66 (2006) 1212–1218.

[9] T. Landete-Castillejos, J.D. Currey, J.A. Estevez, E. Gaspar-López, A. Garcia, L. Gallego, "Influence of physiological effort of growth and chemical composition on antler bone mechanical properties" Bone 41 (2007) 794–803.

[10] F. Bronner, "Metals in bone: Aluminum, boron, cadmium, chromium, lead, silicon, and strontium", Principles of Bone Biology (Second Edition) (2002) 359-369.

[11] G.R. Cointry, R.F. Capozza, A.L. Negri, J.L. Ferretti, "Biomechanical impact of aluminum accumulation on the pre- and post-yield behavior of rat cortical bone" Journal of Bone and Mineral Metabolism 23 (2005) 15–23.

[12] D.M. Medeiros, J. Ilich, J. Ireton, V. Matkovic, L. Shiry, R. Wildman, "Femurs from rats fed diets deficient in copper or iron have decreased mechanical strength and altered mineral composition" The Journal of Trace Elements in Experimental Medicine 10 (1997) 197–203.

[13] J. Ovesen, B. Møller-Madsen, J.S. Thomsen, G. Danscher, Li. Mosekilde, "The positive effects of zinc on skeletal strength in growing rats" Bone 29 (2001) 565–570.

[14] B. Turan, S. Bayari, C. Balcik, F. Severcan, N. Akkas, "A biomechanical and spectroscopic study of bone from rats with selenium deficiency and toxicity" BioMetals 13 (2000) 113–121.

[15] M.M. Brzoska, K. Majewska, J. Moniuszko-Jakoniuk, "Bone mineral density, chemical composition and biomechanical properties of the tibia of female rats exposed to cadmium since weaning up to skeletal maturity", Food and Chemical Toxicology 43 (2005) 1507–1519.

[16] S.M. Besta, A.E. Porterb, E.S. Thiana, J. Huang, "Bioceramics: Past, present and for the future", Journal of the European Ceramic Society 28 (2008) 1319–1327.

[17] J.F. Shackelford, Advanced Ceramics Vol 1: Bioceramics, Overseas Publishers Association (1999) 23–32.

[18] S.J. Kalita, A. Bhardwaj, H.A. Bhatt, "Nanocrystalline calcium phosphate ceramics in biomedical engineering", Materials Science and Engineering C 27 (2007) 441–449

[19] S. Pramanik, A.K. Agarwal, K.N. Rai, A. Garg, "Development of high strength hydroxyapatite by solid-state-sintering process", Ceramics International 33 (2007) 419–426.

[20] S.-H. Rhee, "Synthesis of hydroxyapatite via mechanochemical treatment", Biomaterials 23 (2002) 1147–1152.

[21] G.K. Lim, J. Wang, S.C. Ng, C.H. Chew, L.M. Gan, "Processing of hydroxyapatite via microemulsion and emulsion routes", Biomaterials 18 (1997) 1433-1439.

[22] W.J. Shih, Y.H. Chen, M.C. Wang, M.H. Hon, "Crystal growth and morphology of the nano-sized hydroxyapatite powders synthesized from $CaHPO_4 \cdot 2H_2O$ and $CaCO_3$ by hydrolysis method" Journal of Crystal Growth 270 (2004) 211–218.

[23] H.S. Liu, T.S. Chin, L.S. Lai, S.Y. Chiu, K.H. Chung, C.S. Chang, M.T. Lui, "Hydroxyapatite synthesized by a simplified hydrothermal method", Ceramics International 23 (1997) 19-25.

[24] W. Feng, L. Mu-sen, L. Yu-peng, Q. Yong-xin, "A simple sol–gel technique for preparing hydroxyapatite nanopowders", Materials Letters 59 (2005) 916–919.

[25] M.H. Fathi, A. Hanifi, "Evaluation and characterization of nanostructure hydroxyapatite powder prepared by simple sol–gel method", Materials Letters 61 (2007) 3978–3983.

[26] I. Kim, P.N. Kumt, "Sol–gel synthesis and characterization of nanostructured hydroxyapatite powder", Materials Science and Engineering B 111 (2004) 232–236.

[27] I. Mobasherpour, M.S. Heshajin, A. Kazemzadeh, M. Zakeri, "Synthesis of nanocrystalline hydroxyapatite by using precipitation method", Journal of Alloys and Compounds 430 (2007) 330–333.

[28] T.J. Webster, C. Ergun, R.H. Doremus, R.W. Siegel, R. Bizios, "Enhanced osteoclast-like cell functions on nanophase ceramics", Biomaterials 22 (2001) 1327–1333.

[29] T.J. Webster, C. Ergun, R.H. Doremus, R.W. Siegel, R. Bizios, "Enhanced functions of osteoblasts on nanophase ceramics", Biomaterials 21 (2000) 1803–1810.

[30] R.Z. LeGeros, S. Lin, R. Rohanizadeh, D. Mijares, J.P. LeGeros, " Biphasic calcium phosphate ceramics: Preparation, properties and applications", Journal of Materials Science: Materials in Medicine 14 (2003) 201-209.

[31] S. Sprio, A. Tampieri, E. Landi, M. Sandri, S. Martorana, G. Celotti, G. Logroscino, "Physico-chemical Properties and Solubility Behaviour of Multi-substituted Hydroxyapatite Powders Containing Silicon", Materials Science and Engineering C 28 (2008) 179-187.

[32] M.I. Kay, R.A. Young, A.S. Posner, "Crystal Structure of Hydroxyapatite", Nature 204 (1964) 1050-1052.

[33] Z.Y. Li, W.M. Lam, C. Yang, B. Xu, G.X. Ni, S.A. Abbah, K.M.C. Cheung, K.D.K. Luk, W.W. Lu, "Chemical composition, crystal size and lattice structural changes after incorporation of strontium into biomimetic apatite", Biomaterials 28 (2007) 1452–1460.

[34] http://www.pentax.jp/english/lifecare/newceramics/apaceram/index.html, last visited on 12 January 2009.

[35] L.L. Helson, J. Wilson, "An Introduction to Bioceramics", World Scientific (1993) 139-180.

[36] B. Başar, "Structural, mechanical and biocompatibility investigations of yttrium and fluoride doped nano hydroxyapatite" Masters Thesis, Department of Engineering Sciences, METU, (2009).

[37] G. Bezzi, G. Celotti, E. Landi, T.M.G. La Torretta, I. Sopyan, A. Tampieri, "A novel sol–gel technique for hydroxyapatite preparation", Materials Chemistry and Physics 78 (2003) 816–824.

[38] N.Y. Mostafa, "Characterization, thermal stability and sintering of hydroxyapatite powders prepared by different routes", Materials Chemistry and Physics 94 (2005) 333–341.

[39] A. Banerjee, A. Bandyopadhyay, S. Bose, "Hydroxyapatite nanopowders: Synthesis, densification and cell–materials interaction", Materials Science and Engineering C 27 (2007) 729–735.

[40] E. Fernândez, F.J. Gil, M.P. Ginebra, F.C.M. Driessens, J.A. Planell, S.M. Best, "Calcium phosphate bone cements for clinical applications. Part I: Solution chemistry", Journal of Materials Science: Materials in Medicine 10 (1999) 169-176.

[41] T.J. Webster, E.A. Massa-Schlueter, J.L. Smith, E.B. Slamovich, "Osteoblast response to hydroxyapatite doped with divalent and trivalent cations", Biomaterials 25 (2004) 2111–2121.

[42] C. Ergun, T.J. Webster, R. Bizios, R.H. Doremus, "Hydroxylapatite with substituted magnesium, zinc, cadmium, and yttrium. I. Structure and microstructure", Journal of Biomedical Materials Research 59 (2002) 305–311.

[43] M.E. Fleet, X. Liu, "Site preference of rare earth elements in hydroxyapatite [$Ca_{10}(PO_4)_6(OH)_2$]", Journal of Solid State Chemistry 149 (2000) 391-398.

[44] S.R. Kim, J.H. Lee, Y.T. Kim, D.H. Riu, S.J. Jung, Y.J. Lee, S.C. Chung, Y.H. Kim, "Synthesis of Si, Mg substituted hydroxyapatites and their sintering behaviors", Biomaterials 24 (2003) 1389–1398.

[45] T.J. Webster, C.Ergun, R.H. Doremus, R. Bizios, "Hydroxylapatite with substituted magnesium, zinc, cadmium, and yttrium. II. Mechanisms of osteoblast adhesion", Journal of Biomedical Research 59 (2002) 312-317.

[46] M. Sato, M.A. Sambito, A. Aslani, N.M. Kalkhoran, E.B. Slamovich, T.J. Webster, "Increased osteoblast functions on undoped and yttrium-doped nanocrystalline hydroxyapatite coatings on titanium", Biomaterials 27 (2006) 2358–2369.

[47] H. Eslami, M. Solati-Hashjin, M. Tahriri, "The comparison of powder characteristics and physicochemical, mechanical and biological properties between nanostructure ceramics of hydroxyapatite and fluoridated hydroxyapatite", Materials Science and Engineering C 29 (2009) 1387-1398.

[48] H. Qu, M. Wei, "The effect of fluoride contents in fluoridated hydroxyapatite on osteoblast behavior", Acta Biomaterialia 2 (2006) 113–119.

[49] M.H. Fathi, E.M. Zahrani "Mechanical alloying synthesis and bioactivity evaluation of nanocrystalline fluoridated hydroxyapatite", Journal of Crystal Growth 311 (2009) 1392–1403.

[50] K.A. Gross, L.M. Rodriguez-Lorenzo, "Sintered hydroxyfluorapatites. Part II: Mechanical properties of solid solutions determined by microindentation", Biomaterials 25 (2004) 1385–1394.

[51] H. Kuwahara, N. Mazaki, M. Takahashi, T. Watanabe, X. Yang, T. Aizawa, Mater Sci Eng A 319-321 (2001) 687-691.

[52] B.D. Cullity, "Elements of X-ray Diffraction", Second Edition, Addison-Wesley Publishing Company (1978), Reading, MA, p. 501.

[53] J.E. Hilliard, "Estimating grain size by the intercept method", Metal Progress Data Sheet, (1964) 99-102.

[54] F.A. Barile, "Introduction to in vitro cytotoxicology, mechanisms and methods", CRC Press (1994) 54-55.

[55] http://www.sigmaaldrich.com/life-science/metabolomics/enzyme-explorer/analytical-enzymes/alkaline-phosphatase.html, last visited on 20 December 2009.

[56] I. Lozzi, A. Pucci, O.L. Pantani L.P. D'Acqui, L. Calamai, "Interferences of suspended clay fraction in protein quantitation by several determination methods", Analytical Biochemistry 376 (2008) 108–114.

[57] "G. Lusvardi, G. Malavasi, L. Menabue, V. Aina, C. Morterra, "Fluoride-containing bioactive glasses: Surface reactivity in simulated body fluids solutions" Acta Biomaterialia 5 (2009) 3548–3562

[58] T. Kokubo, H. Takadama, “How useful is SBF in predicting in vivo bone activity”, Biomaterials 27 (2006) 2907–2915.

[59] H. Gitelman, “An improved automated procedure for the determination of calcium in biological specimens”, Analytical Biochemistry 20 (1967) 521-526.

[60] A.S. Kanagasabapathy, S. Kumari, “Guidelines on Standard Operating Procedures for Clinical Chemistry”, Word Health Organization (2000) 59-62.

[61] K.A. Gross, L.M. Rodriguez-Lorenzo, “Sintered hydroxyfluorapatites, part I: Sintering ability of precipitated solid solution powders”, Biomaterials 25 (2004) 1375-1384.

[62] K. Yamashita, H. Owada, H. Nakagawa, T. Umegaki, T. Kanazawa”, Trivalent-cation-substituted calcium oxyhydroxyapatite”, Journal of American Ceramic Society 69 (1986) 590-594.

[63] F. Felsche, “Rare earth silicates with apatite structure”, Journal of Solid State Cemistry 5 (1972) 266-275.

[64] I. Mayer, RS Roth, WE, Brown, “Rare earth substituted fluoride-phosphate apatites”, Journal of Solid State Chemistry 11 (1974) 33-37.

[65] G. Blasse, “Influence of local charge compensation on site occupation and luminescence of apatites”, Journal of Solid State Chemistry 14 (1975) 181-184.

[66] J. Ito, “Silicate apatites and oxyapatites” American Mineralogist 53 (1968) 890-907.

[67] P.E. Wang, T.K. Chaki, “Mechanical Properties of Sintered Calcium Phosphates”, Bioceramics: Materials and Applications / edited by G. Fischman, A. Clare, L. Hench, Ceramic Transactions 48 (1995) 225-234.

[68] S. Ramesh, C.Y. Tan, S.B. Bhaduri, W.D. Teng, I. Sopyan, “Densification behaviour of nanocrystalline hydroxyapatite bioceramics”, Journal of Materials Processing Technology 206 (2008) 221-230.

[69] H. Qu, M. Wei, “Effect of fluorine content on mechanical properties of sintered hydroxyapatite”, Materials Science and Engineering C 26 (2006) 46-53.

[70] Z.Y. Li, W.M. Lam, C. Yang, B. Xu, G.X. Ni, S.A. Abbah, K.M.C. Cheung, K.D.K. Luk, W.W. Lu, "Chemical composition, crystal size and lattice structural changes after incorporation of strontium into biomimettic apatites" Biomaterials 28 (2007) 1452–1460.

[71] H.W. Kim, E.J. Lee, H.E Kim, V. Salih, J.C. Knowles, "Effect of fluoridation of hydroxyapatite in hydroxyapatite-polycaprolactone composites on osteoblast activity" Biomaterials 26 (2005) 4395–4404.

[72] J. Wang, Y. Chao, Q. Wan, Z. Zhu, H. Yu, "Fluoridated hydroxyapatite coatings on titanium obtained by electrochemical deposition", Acta Biomaterialia 5 (2009) 1798–1807.

[73] K. Cheng, W. Weng, H. Wang, S. Zhang, "In vitro behavior of osteoblast-like cells on fluoridated hydroxyapatite coatings ",Biomaterials 26 (2005) 6288–6295.

[74] J.R. Farley, J.E. Wergedal, D.J. Baylink, "Fluoride directly stimulates proliferation and alkaline phosphatase activity of bone-forming cells" Science 222 (1983) 330-332.

[75] Z. Shi, X. Huang, Y. Cai, R. Tang, D. Yang, Size e*ff*ect of hydroxyapatite nanoparticles on proliferation and apoptosis of osteoblast-like cells Acta Biomaterialia 5 (2009) 338–345.

[76] T.J. Webster, R.W. Siegel, R. Bizios, "Osteoblast adhesion on nanophase ceramics" Biomaterials 20 (1999) 1221-1227.

[77] Guyton, A.C., 1991, Textbook of Medical Physiology, 8th ed. W.B. Saunders Company, Philadelphia.

[78] Y. Wang, S. Zhang, X. Zeng, L.L. Ma, W. Weng, W. Yan, M. Qian, "Osteoblastic cell response on fluoridated hydroxyapatite coatings" Acta Biomaterialia 3 (2007) 191–197.

[79] B.H. Yoon, H.W. Kim, S.H. Lee, C.J. Bae, Y.H. Koh, Y.M. Kong, H.E. Kim, "Stability and cellular responses to fluorapatite–collagen composites", Biomaterials 26 (2005) 2957–2963.

[80] L. Zhu, A.I. Skoultchi, "Coordinating cell proliferation and differentiation", Current Opinion in Genetics & Development 10 (2001) 91–97.

[81] Y. Wan, S. Zhang, X. Zeng, K. Cheng, M. Qian, W. Weng, "In vitro behavior of fluoridated hydroxyapatite coatings in organic-containing simulated body fluid" Materials Science and Engineering C 27 (2007) 244-250.

[82] S. Ma, Y. Yang, D.L. Carnes, K. Kim, S. Park, S.H. Oh, Effects of dissolved calcium and phosphorous on osteoblast responses" Journal of Oral Implantology 31 (2005) 61–67.

[83] Boyan B.D., Lohmann C.H., Dean D.D., Sylvia V.L., Cochran D.L., Schwartz Z., "Mechanisms involved in osteoblast response to implant surface morphology" Annual Review of Materials Research 31 (2001) 357–71.

[84] Kartsogiannis V, Ng KW. "Cell lines and primary cell cultures in the study of bone cell biology" Molecular and Cellular Endocrinology 228 (2004) 79–102.

APPENDIX A

CALIBRATON CURVE FOR ALP ACTIVITY ASSAY

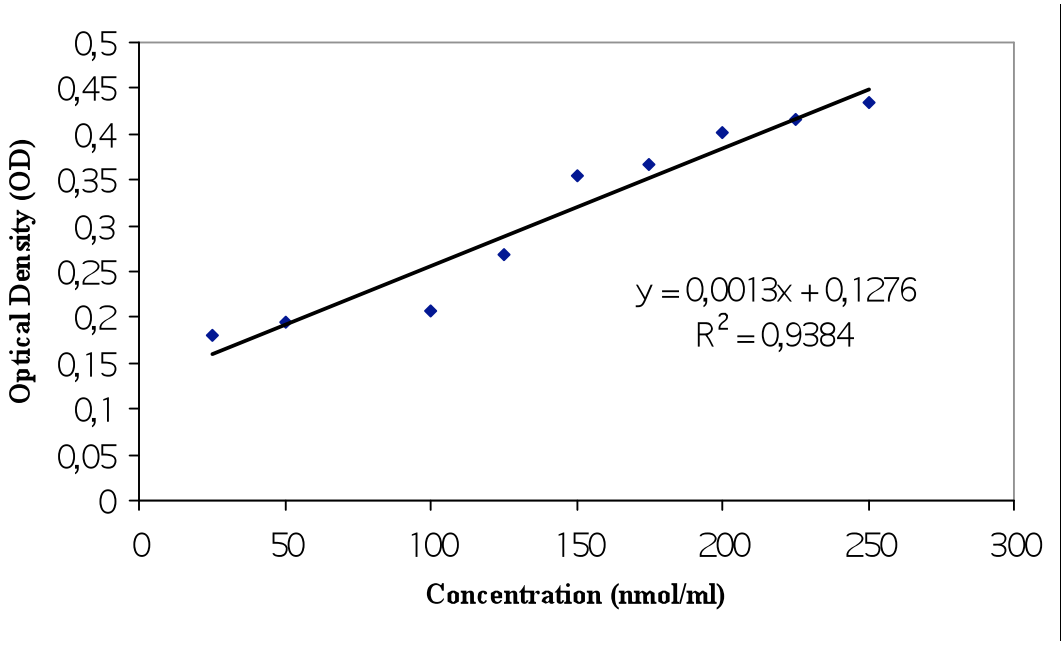

Figure A.1. The calibration curve of p-nitrophenol.

APPENDIX B

CALIBRATON CURVE FOR BCA ASSAY

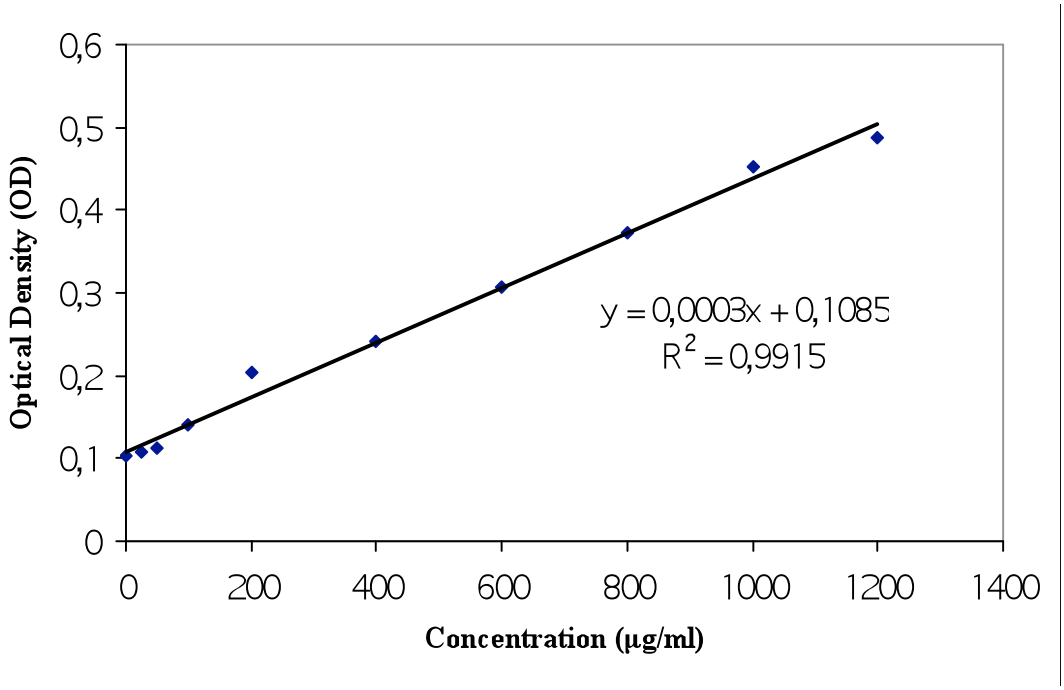

Figure B.1. The calibration curve of bovine serum albumin.

APPENDIX C

CALIBRATON CURVE FOR CALCIUM CONCENTRATION IN DISSOLUTION TEST

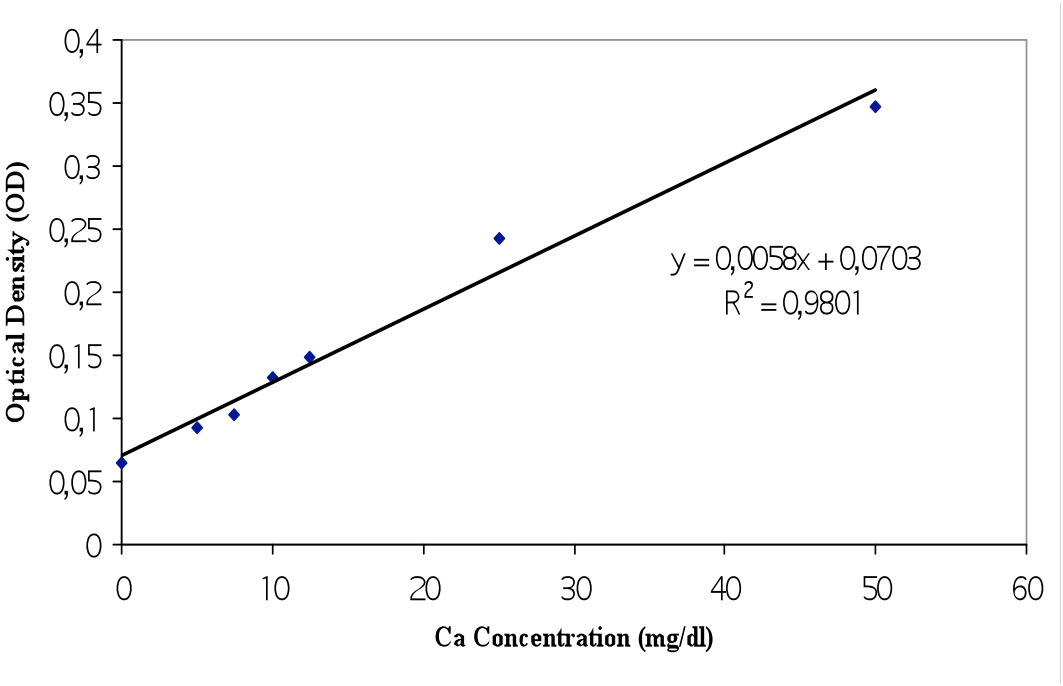

Figure C.1. The calibration curve of calcium carbonate.